

JGR Solid Earth

RESEARCH ARTICLE

10.1029/2019JB018088

Key Points:

- Seismicity correlates with tidal normal stress rather than tidal shear stress
- Earthquakes tend to occur when the tidal stress levels have large positive values and tend to be suppressed when large negative values
- Gutenberg-Richter b value decreases when the tidal stress difference is high

Supporting Information:

- Supporting information S1
- Table S1

Correspondence to:

F. Hirose,
fhirose@mri-jma.go.jp

Citation:

Hirose, F., Maeda, K., & Kamigaichi, O. (2019). Tidal forcing of interplate earthquakes along the Tonga-Kermadec Trench. *Journal of Geophysical Research: Solid Earth*, 124, 10,498–10,521. <https://doi.org/10.1029/2019JB018088>

Received 30 MAY 2019

Accepted 27 SEP 2019

Accepted article online 14 OCT 2019

Published online 25 OCT 2019

Tidal Forcing of Interplate Earthquakes Along the Tonga-Kermadec Trench

Fuyuki Hirose¹ , Kenji Maeda² , and Osamu Kamigaichi³

¹Seismology and Tsunami Research Department, Meteorological Research Institute, Tsukuba, Japan, ²Seismology and Volcanology Department, Japan Meteorological Agency, Chiyoda-ku, Japan, ³Meteorological College, Japan Meteorological Agency, Kashiwa, Japan

Abstract We investigated the spatiotemporal variations of the relation between the levels and phase angles of Earth tidal indices and the occurrence of interplate earthquake events along the Tonga-Kermadec trench. As tidal indices, we used volumetric strain (ΔV), shear stress ($\Delta\tau$), normal stress ($\Delta\sigma$), and the Coulomb failure function (ΔCFF ; calculated assuming values of 0.1, 0.4, and 0.7 for the apparent friction coefficient, μ'). We found that seismicity correlated with $\Delta\sigma$ rather than $\Delta\tau$ and that earthquakes tended to occur when the tidal force promoted fault slip. Earthquakes tend to occur when the tidal stress levels have large positive values and tend to be suppressed when large negative values. We inferred that μ' is relatively large on the plate boundary along the Tonga-Kermadec trench, which implies that the response of pore pressure to $\Delta\sigma$ is weak. Seismicity at around 20–22°S and 27–29°S was particularly sensitive to $\Delta\sigma$. The b value of the Gutenberg-Richter relation decreased when the difference between the maximum and minimum tidal principal stresses was high, consistent with the results of rock deformation experiments.

1. Introduction

Tidal stress can influence seismicity at various scales, from low-frequency tremors to great earthquakes (e.g., Ide et al., 2016; Ide & Tanaka, 2014; Tanaka et al., 2002a). Tanaka et al. (2002a) investigated the relation between tidal stress changes and the occurrence of 9,350 globally distributed earthquakes with $M_w \geq 5.5$ listed in the Harvard centroid moment tensor catalog for the period 1977–2000, and found a high correlation between the shear stress change and the occurrence of shallow, reverse fault-type earthquakes with $M_w < 7.0$. Moreover, they reported that earthquakes tended to occur just before the tidal shear stress reached its maximum. Ide and Tanaka (2014) found that deep tremor activity offshore of Okayama Prefecture, Japan, was associated with low tide levels. In addition, they pointed out that the occurrences of low-frequency tremors, background seismicity, and large earthquakes along the Nankai trough during the past 1,400 years were correlated with the 18.61-year cycle of lunar motion. Ide et al. (2016) investigated the relation between the maximum tidal shear stress and 11,397 events with $M_w \geq 5.5$ that occurred globally during 1976–2015 and found that 75% ($=9/12$) of earthquakes with $M_w \geq 8.2$ occurred on days when the daily maximum tidal shear stress amplitude was in the top third of the 15 days preceding the main shock. These findings indicate that temporal variations in tidal stress on the order of kilopascals can affect slip on a plate boundary, suggesting that tidal stress variations might provide a physical basis for estimating temporal variations in earthquake occurrence probability.

The Tonga-Kermadec trench (Tt and Kt in Figure 1a) is a very seismically active area, and is thus suitable for investigating the relation between seismicity and tides. Previous study (Tanaka et al., 2002b) reported that p value which was an index of correlation between tides and earthquakes (see section 3 for details) decreased before the 1982 Tong earthquake of $M7.5$ and increased after it. Thus, the p value is considered a promising tool to forecast large earthquakes. In the more than 10 years since their study, the total number of earthquakes available to study has doubled. $M7$ -class earthquakes have occurred frequently. We investigated preliminarily the temporal variations of the p value before and after these $M7$ -class earthquakes. As a result, we could not find the decrease of the p value before them except the 1982 event, and we are preparing another manuscript on this issue. Furthermore, the p value is dependent only on the tidal phase angle (see section 3 for the definition), and amplitude information is not considered, which we consider is also important, such as in Ide et al. (2016). Therefore, in this study we focused on investigation into fundamental characteristics of

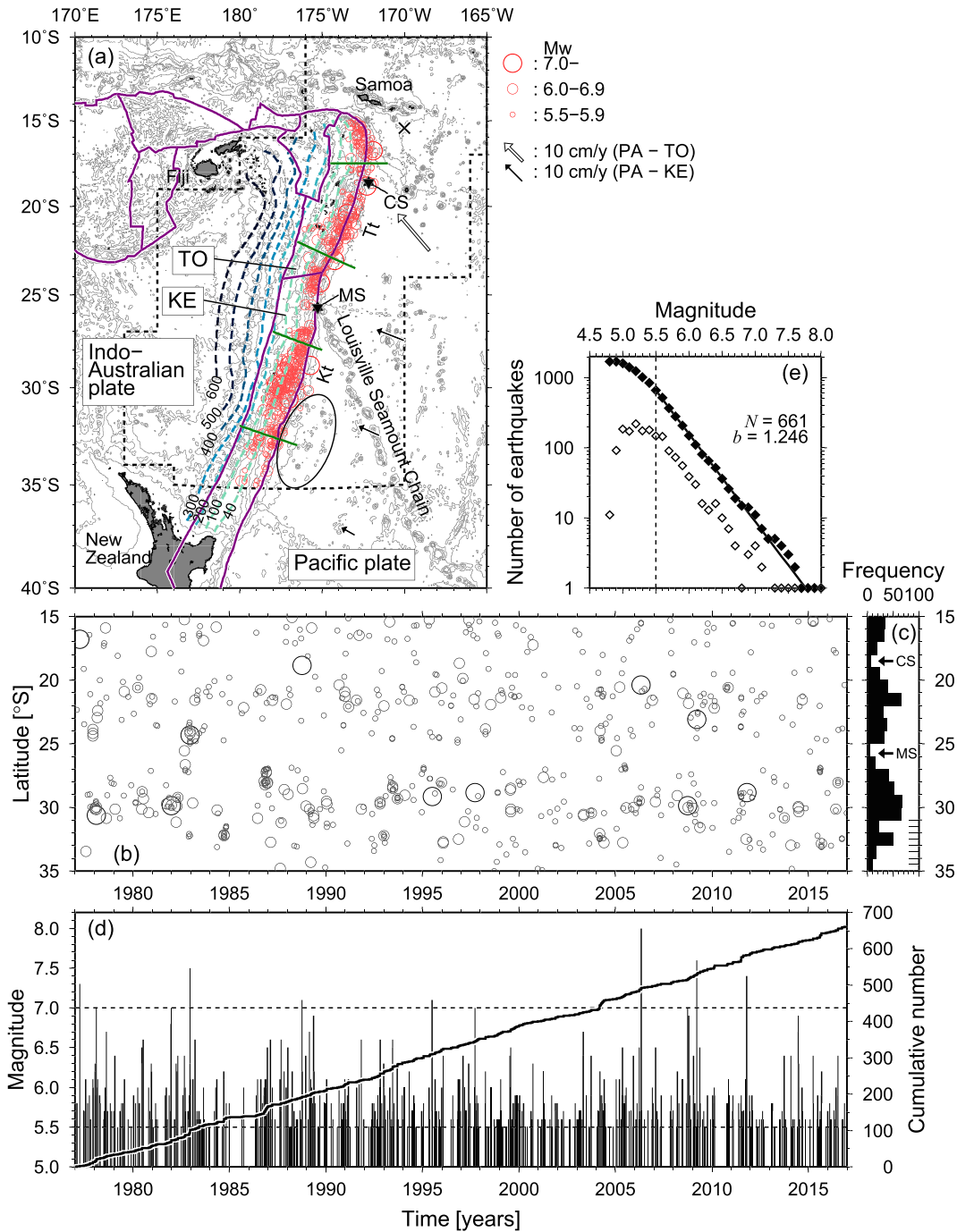


Figure 1. (a) Epicenter distribution of 661 shallow interplate (thrust) earthquakes (focal depth ≤ 70 km, $M_w \geq 5.5$) that occurred in the Tonga-Kermadec region from 1 January 1977 to 31 December 2016. A cross near 16.5°S, 170°W denotes an excluded event (see text). The purple line denotes the plate boundary at the Earth's surface (Bird, 2003). Colored contours with numerals in (a) represent depth in kilometers of the upper surface of the subducting Pacific slab (Hayes et al., 2012). The studied area, within the dashed line, is the same as that of Tanaka et al. (2002b). The white and black arrows indicate the movement of the Pacific plate (PA) relative to the Tonga plate (TO) and to the Kermadec plate (KE), respectively. Tt and Kt denote the Tonga trench and the Kermadec trench, respectively. The two hexagrams indicate the centers of the Capricorn seamount (CS) and Mo'unga seamount (MS). The ellipse represents a cluster of petite seamounts on the outer rise. Green lines show the locations of vertical cross sections in Figure 2. (b) Time-space plot of earthquake focal mechanisms. (c) Earthquake frequency per degree of latitude. CS and MS denote locations of the Capricorn and Mo'unga seamounts, respectively. The thin bars at the bottom right represent seamounts on the outer rise. (d) Plot of earthquake magnitudes (vertical bars) and the cumulative number of earthquakes (curve) versus time. (e) Magnitude frequency distribution of shallow thrust events in the studied area. Open diamonds denote the number of events in each magnitude bin, and solid diamonds denote the cumulative number. The line is the fitted distribution of the Gutenberg-Richter law (Gutenberg & Richter, 1944) for $N = 661$ and $b = 1.246$.

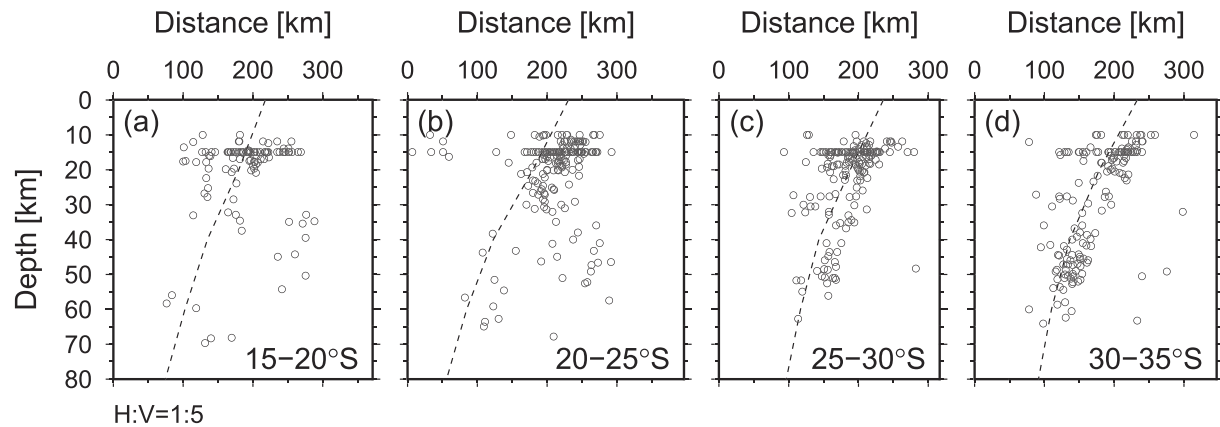


Figure 2. Vertical cross section along the green lines in Figure 1a. Broken lines are the plate boundary (Hayes et al., 2012). Earthquakes within $\pm 2.5^\circ$ of latitude from each line are plotted in each panel.

the correlation between Earth tides and interplate earthquakes in this area using recent seismic data and the information of not only tidal phase angles but also amplitude. In addition, we more carefully evaluated ocean tidal loading contributions from near distances from the epicenter by increasing the number of calculation points on which the values of green function from surface vertical loading (see section A3) are given than the previous study (Tanaka et al., 2002b). We found clearly that tidal normal stress contributes to the triggering of earthquakes more than tidal shear stress, as pointed out by Tanaka et al. (2002b). We also touch upon a disadvantage of using the p value method only.

2. Data

We extracted 661 interplate type earthquakes (strike angle $150\text{--}230^\circ$, rake angle $55\text{--}125^\circ$, depth $0\text{--}70$ km, and $M_w \geq 5.5$) from the Global Centroid Moment Tensor (GCMT) catalog (Dziewonski et al., 1981; Ekström et al., 2012) that occurred from 1977 through 2016 (Figure 1 and Table S1). We set the range of strike angles ($150\text{--}230^\circ$) by considering the $180\text{--}200^\circ$ strike of the Tonga-Kermadec trench and the error of the GCMT solutions ($\pm 30^\circ$). Our studied area (within the dashed line in Figure 1a) is the same as that of Tanaka et al. (2002b) based on the regionalization of Flinn et al. (1974). To include the largest event (M_w 8.0, rake angle 123°) that occurred near 20°S in May 2006, we used a wider range of rake angles than that ($60\text{--}120^\circ$) used by Tanaka et al. (2002b). Event selection criteria $M_w \geq 5.5$ is higher enough than a detection threshold as seen from magnitude frequency distribution (Figure 1e). No events with $M_w \geq 5.5$ had hypocenters shallower than 10 km (Figure 2). The number of earthquakes was clearly lower in the latitudinal intervals $18\text{--}19^\circ\text{S}$, $25\text{--}26^\circ\text{S}$, and $31\text{--}35^\circ\text{S}$ (Figure 1c). The $18\text{--}19^\circ\text{S}$ interval apparently corresponds to the Capricorn Seamount (Crawford et al., 2003), and the $25\text{--}26^\circ\text{S}$ interval seems to correspond to the subducting Mo'unga Seamount (Ballance et al., 1989) of the Louisville seamount chain. The $31\text{--}35^\circ\text{S}$ interval may correspond to a spatial range of a cluster of petite seamounts on the outer rise. The number of earthquakes per degree of latitude in the three sections bounded by these low-seismicity areas increases southward (29 earthquakes/degree in $15\text{--}18^\circ\text{S}$, 38/degree in $19\text{--}25^\circ\text{S}$, and 48/degree in $26\text{--}31^\circ\text{S}$). Interplate type earthquakes have occurred intermittently including clear quiescence around 1985 (Figure 1d).

The accuracy of hypocenter determination is low in this area and there are many earthquakes fixed at the depth of 15 km (Figure 2). Earthquakes that satisfy the selection condition shown above in this section, which correspond to the interplate type focal mechanism, do not always distribute along the plate boundary estimated by Hayes et al. (2012) (Figure 2). However, we assume that these earthquakes are interplate earthquakes after the previous study (Tanaka et al., 2002b) relying on the focal mechanism. The information of the hypocenter and the occurrence time of each event in the GCMT catalog was used to calculate the theoretical tidal response.

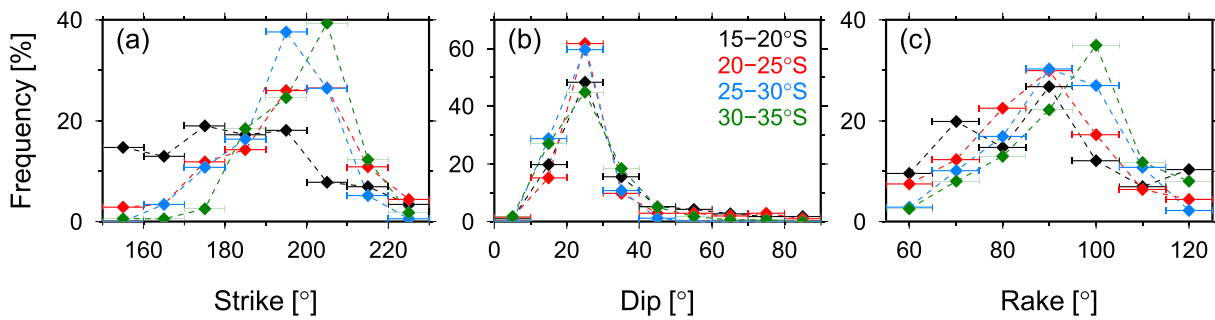


Figure 3. Distribution of fault parameters: (a) strike, (b) dip, and (c) rake angles. Colors of symbols correspond to sections shown in (b).

Although the M_w 6.1 event near 16.5°S, 170°W in October 2003 (a cross in Figure 1a) satisfies the conditions indicated above, we excluded it from this study because it was clearly an intraplate earthquake that occurred in the Pacific plate far from the trench.

Figure 3 shows the distribution of fault parameters of earthquakes within the four sections divided in the north-south direction. There were many earthquakes with strike angles of 150–200° at the northern part and 190–210° at the southern part (Figure 3a). Dip angles in all sections had a peak in 20–30° (Figure 3b). As for the rake angle (Figure 3c), it shows two peaks in 65–75° and 85–95° at the northern part. There is a peak in 85–95° at the middle part and 95–105° at the southern part.

3. Method

The theoretical belowground tidal response, expressed as the summation of solid tide (direct term) and ocean tide (indirect term) loading effects, is often called the Earth tide (“tide” hereafter). Here, the solid and ocean tide loading effects were estimated separately (see section A1). For a more elaborate evaluation of the tidal loading effect especially from near distance from the epicenter, we increased the number of calculation points in a short range on which the values of green function from surface vertical loading (see section A3) are given than the previous study (Tanaka et al., 2002b), because the contribution from short range from an epicenter is dominant for stress and strain.

We summed temporal variations of the solid and oceanic tide loading effects for six independent components of the strain tensor, as estimated at the hypocenter of each event. We set the sampling interval at 3 min that obtained higher temporal resolution than the previous study (Tanaka et al., 2002b). Then we converted them to temporal variations of volumetric strain (ΔV) at the hypocenter, and shear stress ($\Delta\tau$), normal stress ($\Delta\sigma$), and the Coulomb failure function (ΔCFF) on the assumed fault plane based on the GCMT solution extracted in section 2 (see section A4). In the ΔCFF calculation, we assumed values of 0.1, 0.4, and 0.7 for the apparent friction coefficient μ' (hereafter $\Delta CFF_{(0.1)}$, $\Delta CFF_{(0.4)}$, and $\Delta CFF_{(0.7)}$, respectively). In the case of ΔV and $\Delta\sigma$, we defined expansion/dilatation as positive and contraction/compression as negative; consequently, positive $\Delta\sigma$ values promote fault slip. We also defined $\Delta\tau$ and ΔCFF as positive when they promote fault slip. In this study, we examined these six tide-related indices (hereafter “tidal indices”; i.e., ΔV , $\Delta\tau$, $\Delta\sigma$, $\Delta CFF_{(0.1)}$, $\Delta CFF_{(0.4)}$, and $\Delta CFF_{(0.7)}$) in relation to the timing of earthquake events.

Figure 4 shows examples of the theoretical tidal responses of $\Delta\tau$ and $\Delta\sigma$ during two days centered on the occurrence time of the 1982 event of $M7.5$. A large contribution of solid tide for $\Delta\tau$ and the ocean tide for $\Delta\sigma$ (Figures 4a and 4b) can be seen. We used the ocean tide model NAO.99b (Matsumoto et al., 2000) for the 16 major constituents in short-period bands (M2, S2, K1, O1, N2, P1, K2, Q1, M1, J1, OO1, 2N2, Mu2, Nu2, L2, T2) and model NAO.99L (Takanezawa et al., 2001) for the five constituents in long-period bands (Mtm, Mf, Mm, Ssa, Sa; see section A1.2). Among 21 constituents, the contribution of the five constituents in long-period bands is very small (LONGP in Figures 4c and 4d) and the contribution of the 16 constituents in short-period bands is large (SHORTP in Figures 4c and 4d). Among SHORTP, the contribution of the eight major constituents is large (M2, S2, K1, O1, N2, P1, K2, Q1: MAJOR8 in Figures 4c and 4d). Furthermore, among MAJOR8, M2 constituent which is principal lunar semidiurnal tide is dominant (Figures 4e and 4f).

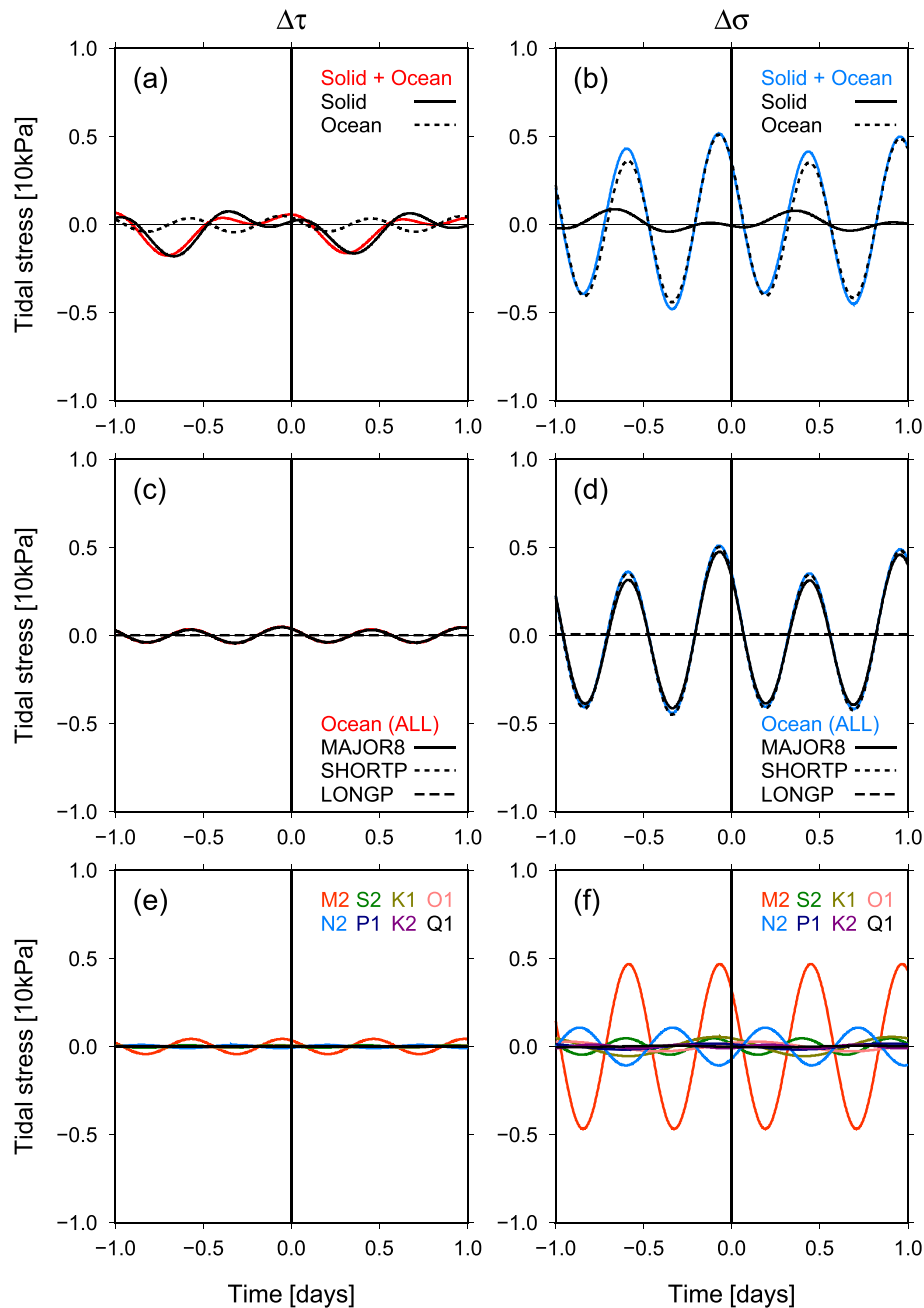


Figure 4. Examples of temporal variations of solid tide and ocean tide loading effects: (a, c, and e) shear stress $\Delta\tau$ and (b, d, and f) normal stress $\Delta\sigma$. Plotted period starts 1 day before the event occurrence time and ends 1 day after: 19 December 1982 at 17:44 UTC (M_w 7.5, depth: 29.2 km, strike: 198°, dip: 22°, and rake: 101°). (a and b) The contribution of solid tide (solid curves) and ocean tide loading effects (broken curves) to the summation (red or blue). (c and d) The contribution of constituents to ocean tide loading effects. Solid curves denote the eight major constituents (M2, S2, K1, O1, N2, P1, K2, Q1), short broken curves denote the 16 major constituents in short-period bands (M2, S2, K1, O1, N2, P1, K2, Q1, M1, J1, OO1, 2N2, Mu2, Nu2, L2, T2), and long broken curves denote the five constituents in long-period bands (Mtm, Mf, Mm, Ssa, Sa). Red and blue curves denote the 21 constituents, and are the same as broken curves in (a) and (b), respectively. (e and f) The contribution of the eight major constituents.

We assigned a tidal phase angle and tidal stress (strain) level to each event in accordance with previous studies (e.g., Tsuruoka et al., 1995) as follows (Figure 5). The tidal stress (strain) level at the earthquake occurrence time was defined as the tidal index value measured from the zero line to emphasize the significance of its sign (positive or negative) in the discussion below. Using the time series of tidal stress (strain) levels, we assigned phase angles of -180° and 180° to the minimum tidal stress (strain) levels before and

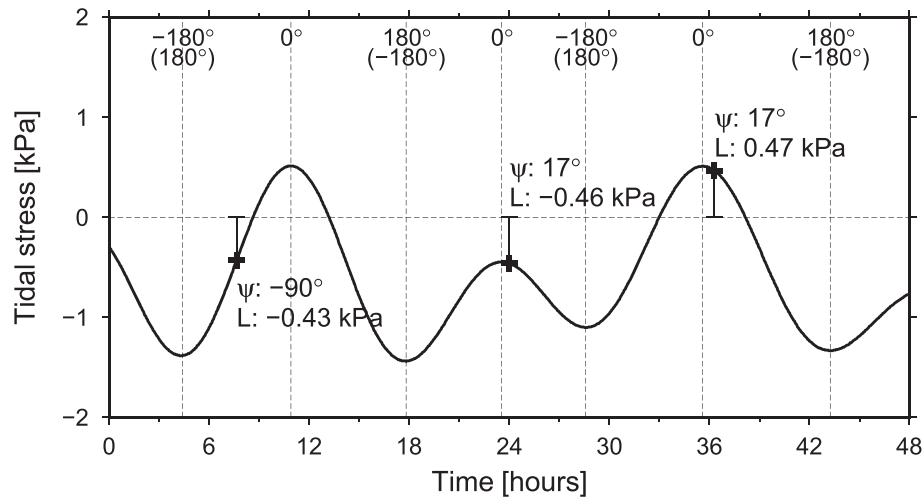


Figure 5. Estimation of phase angles (ψ) and tidal index levels (L) at earthquake occurrence times (crosses) from the temporal variations in tidal index values. The example shown is for “tidal shear stress,” and the same procedure was used for all six tidal indices.

after an event, respectively, and 0° to the maximum tidal stress (strain) that occurred between these two minima. The phase angle at the earthquake occurrence time was estimated by linear interpolation in the time interval between -180° and 0° or between 0° and 180° .

The possible occurrence of earthquakes at certain tidal phase angles is often evaluated using the p value, as calculated by Schuster (1897):

$$p = \exp\left(-\frac{D^2}{N}\right), \quad (1)$$

$$D = \sqrt{\left(\sum_{i=1}^N \cos\psi_i\right)^2 + \left(\sum_{i=1}^N \sin\psi_i\right)^2}, \quad (2)$$

where N is the total number of earthquakes and ψ_i is the phase angle of the i th earthquake. D in equation (2) indicates the final distance from the origin through two-dimensional random walk of N steps. Equation (1) is the complementary cumulative distribution function of the Rayleigh distribution and corresponds to the probability that the magnitude of the vector sum of a random set of earthquake phase angles will be greater than D . Note that the approximation of equation (1) is sufficient only when N is larger than 10 (Heaton, 1975). Thus, the p value represents the significance level for rejecting the null hypothesis that earthquakes occur randomly with respect to the tidal phase angle, and ranges between 0 and 1 (or between 0 and 100%), such that the confidence in rejecting the null hypothesis becomes greater as the p value becomes smaller. In general, the value of 5% is often used as a standard value of p to judge tidal correlation (e.g., Tanaka et al., 2002a), and is also adopted in this study.

Here, we examine the property of the p value. Figure 6 shows examples of imaginary frequency distributions of 661 synthetic tidal phase angles which have a center value in each bin (e.g., -10° in the section of -20° – 0°). Firstly, in Figures 6a–6c, frequencies in the section of -20° – 0° stand out. However, only the p value in Figure 6c shows less than 5%. Even if the frequencies in the section of -20° – 0° and others have about 2 times difference ($=9.98/5.30$), the p value becomes more than 5% (Figure 6b). In Figure 6d, frequencies in the sections of -180° – -140° and 140° – 180° are decreased and those in the sections of -60° – -20° and 0° – 40° are increased in the same amount from Figure 6a. The p value becomes 4.23%, indicating significant tidal correlation. In Figure 6e, frequency in the section of -180° – -100° is decreased and that in the section of -100° – -20° is increased in the same amount from Figure 6a. The p value becomes 3.90%, indicating significant tidal correlation also. In Figure 6f, frequencies in the sections of -160° – -20° and 0° – 180° are decreased and that in the section of -180° – -160° is increased in the same amount from Figure 6c. Although the frequency in the section of -20° – 0° stands out more compared to Figure 6c, the frequency in the section of

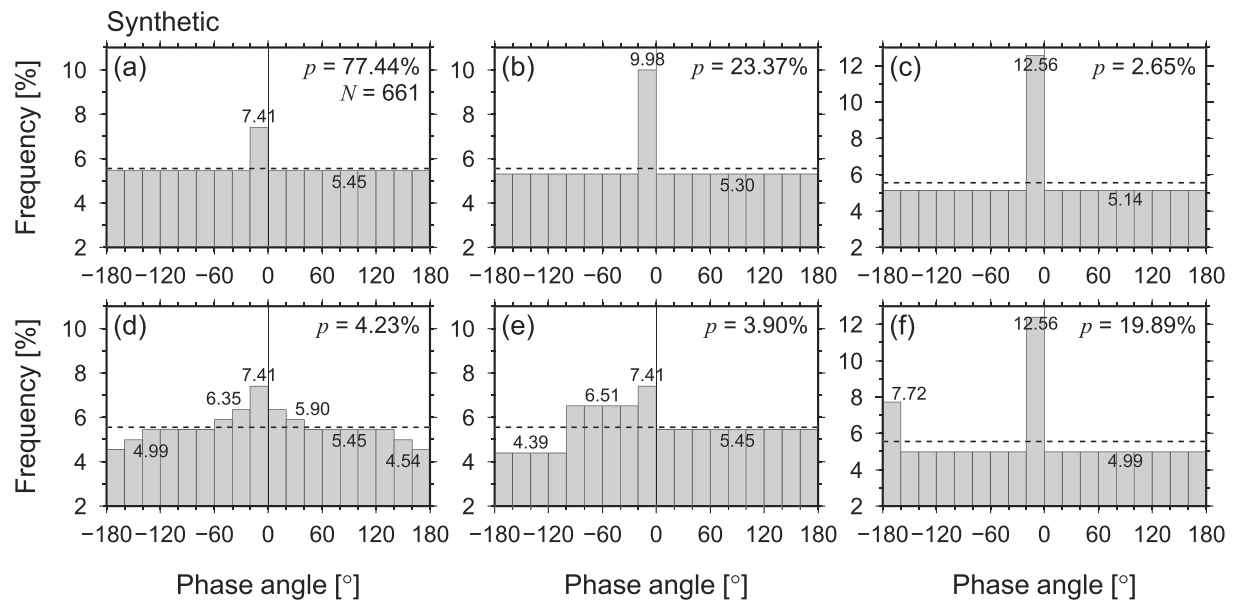


Figure 6. Examples of frequency distributions of 661 synthetic tidal phase angles. The broken horizontal line in each panel represents the mean frequency (100%/18).

−180−160° having the phase angle difference of 160° has also a local peak, resulting in the p value of 19.89%, indicating no tidal correlation. According to these, to make p value small, not only a large frequency in the specific section but also small frequencies in other sections having the opposite phase angle are necessary. Fitting a sinusoidal curve to the phase angle frequency distribution can be an equivalence of the p value method (e.g., Tanaka et al., 2002a). The p value is an index that takes not only the promotion (tidal triggering) but also the suppression of earthquakes into consideration.

However, care must be taken when two phase angle frequency distributions show similar p values but their distributions are reverse to each other. In this case, both tidal indices would be regarded to have similar correlation to earthquake occurrence. Now we have the information of not only tidal phase angles but also stress levels. There is physically contradictory even though the p value is small if the frequency distribution of earthquakes reaches a maximum when the tidal force suppresses fault slip. Thus, we can judge that no tidal correlation exists between that index and seismicity. It is worth to use the information of tidal stress levels.

In calculation of the theoretical tidal response just at the depth of the physical property boundary in the Earth model, our calculation program uses the physical property in the upper layer (see section A2). On the other hand, calculation logic of Tanaka et al. (2002a, 2002b) uses the physical property in the lower layer. As shown in Figure 2, the accuracy of hypocenter determination is low in this area and there are many earthquakes (207 events) fixed at the depth of 15 km that corresponds to the depth of the physical property boundary. When we compared the former case with the latter case for earthquakes at the depth of 15 km, phase angles of $\Delta\sigma$ of both cases were much the same each other (2° difference at most) while those of $\Delta\tau$ were greatly different (113 events among 207 events, about 55%, had phase angle difference with more than 20°). Accordingly, the difference between tidal phase angle distributions of our study and that of the previous study (Tanaka et al., 2002b) depends on not only the loading green function, calculation mesh size, and temporal resolution (our study has higher resolution than the previous study) but also the treatment for earthquakes occurring on the physical property boundary. However, we confirmed that our conclusion that interplate type earthquakes along the Tonga-Kermadec trench correlated with $\Delta\sigma$ rather than $\Delta\tau$ (see below) does not change even if we adopted the physical property in the lower layer.

4. Results

Figure 7 shows examples of the theoretical tidal responses during two days centered on the occurrence times of the three largest (M_w 7.5, 8.0, 7.6) among the 661 events. The changes in volumetric strain (green lines) and

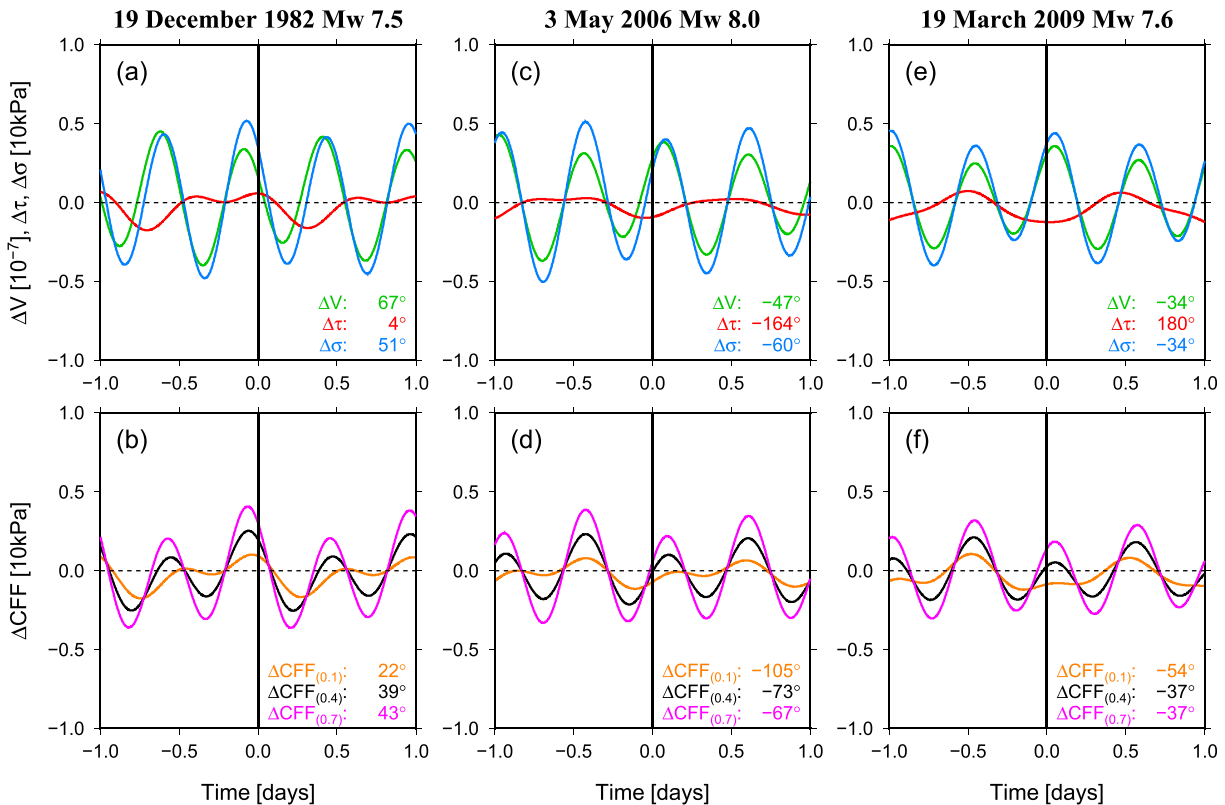


Figure 7. Examples of tidal index variations: (green) volumetric strain ΔV , (red) shear stress $\Delta \tau$, (blue) normal stress $\Delta \sigma$, (orange) ΔCFF with $\mu' = 0.1$, (black) ΔCFF with $\mu' = 0.4$, and (purple) ΔCFF with $\mu' = 0.7$. Each plotted period starts 1 day before the event occurrence time and ends 1 day after: (a and b) 19 December 1982 at 17:44 UTC (M_w 7.5), (c and d) 3 May 2006 at 15:27 UTC (M_w 8.0), and (e and f) 19 March 2009 at 18:17 UTC (M_w 7.6). The estimated tidal phase angles are shown at the bottom right in each panel.

normal stress (blue lines) are very similar, which is also expected by the theoretical formula (see equation (A6) in Appendix A4). The characteristics of the shear stress time series are different from those of the other tidal indices. Because shear stress amplitudes are about 1/10 to 1/5 of the normal stress amplitudes, the contributions of shear stress and normal stress to ΔCFF are equivalent when $\mu' = 0.1$ –0.2. However, when $\mu' > 0.2$, the contribution of normal stress to ΔCFF becomes dominant. Tidal stress levels of $\Delta \sigma$ (blue) show to be positive at the three events, indicating that earthquakes occurred when tidal stresses promote fault slip. For $\Delta \tau$ (red), the 1982 earthquake also occurred when tidal stress level was positive. On the other hand, the 2006 and 2009 earthquakes occurred when tidal stress levels of $\Delta \tau$ became negative. This indicates that earthquakes occurred when tidal stresses suppress fault slip, indicating no contribution to tidal triggering. Tidal phase angles at the event occurrence time estimated using each tidal index are shown at the bottom right of each panel in Figure 7. We can see the periodicity about 12 and 24 hr in $\Delta \sigma$ (and ΔV and $\Delta CFF_{(0.4, 0.7)}$ having a high similarity to $\Delta \sigma$ by definition). On the other hand, $\Delta \tau$ shows 24-hr cycle mainly, and those tidal phase angles differ from other components. Tidal phase angles of $\Delta CFF_{(0.1)}$ show the roughly average of those of $\Delta \sigma$ and $\Delta \tau$ to $\Delta CFF_{(0.1)}$ are equivalent.

In order to find out comprehensive characteristics, we investigated the relations between tidal phase angles at the occurrence times of all 661 events as estimated by different tidal indices (Figure 8). The result, firstly, showed that the differences in tidal phase angles estimated using ΔV , $\Delta \sigma$, $\Delta CFF_{(0.4)}$, and $\Delta CFF_{(0.7)}$ were small (Figures 8a–8c, 8f, 8g, and 8j), indicating that $\Delta \sigma$ represents well ΔV , $\Delta CFF_{(0.4)}$, and $\Delta CFF_{(0.7)}$. Next, Figure 8i shows the correlation between $\Delta \sigma$ and $\Delta \tau$, and it shows a significant scatter (the correlation coefficient is 0.27). But still, some positive trends with some constant phase shifts can be seen, probably because M2 constituent is dominant both in $\Delta \sigma$ and $\Delta \tau$ (Figures 4e and 4f). Finally, $\Delta CFF_{(0.1)}$ has moderate correlations with $\Delta \sigma$ (Figure 8h) and $\Delta \tau$ (Figure 8o). Accordingly, six tidal indices can be represented by $\Delta \sigma$, $\Delta \tau$, and $\Delta CFF_{(0.1)}$. Hereafter, we show results of these three components mainly.

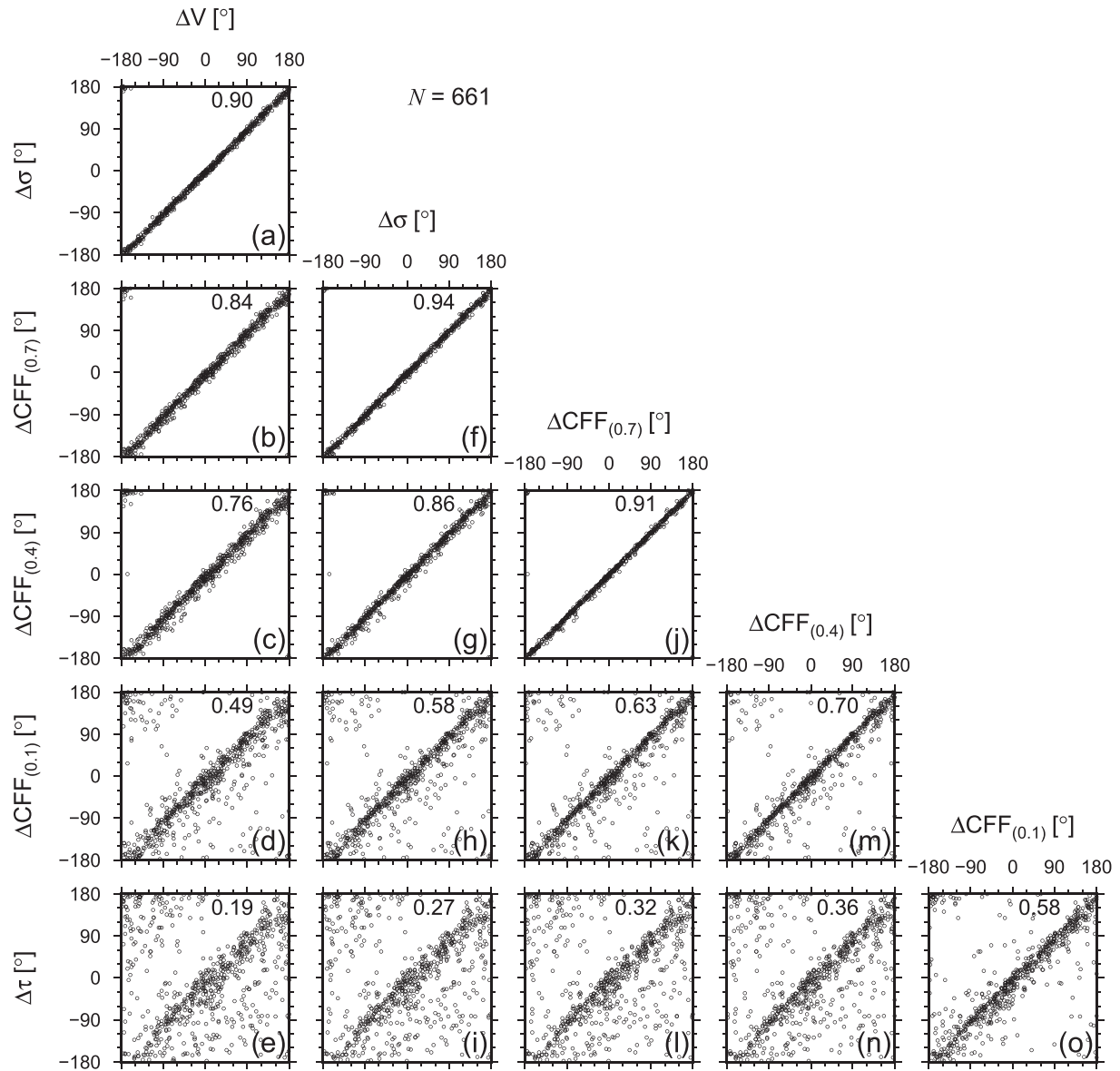


Figure 8. Correlations of tidal phase angles estimated using different tidal indices. The correlation coefficient is shown at the top in each panel.

We also examined the relations between tidal phase angles and tidal index levels (Figure 9). For example, $\Delta\sigma$ levels tended to be positive when phase angles ranged from -90° to 90° , and negative otherwise (Figure 9b). Levels of $\Delta\tau$ and $\Delta\text{CFF}_{(0.1)}$ (Figures 9a and 9c), however, were sometimes negative even at phase angles of -90° to 90° ; thus, the relations between tidal index levels and phase angles were not always linear. At tidal phase angles near the local maximum (0°) or minimum ($\pm 180^\circ$), stress levels tended to be scattered (Figures 9d–9f). In light of these results, we considered that use of the tidal phase angle alone might not be adequate for the aims of this study, so we used both the phase angle and the levels of the tidal indices to arrive at a more comprehensive interpretation of the relation between tides and seismicity.

5. Discussion

5.1. Characteristics of Tidal Phase Angles

Figure 10 shows the frequency distribution of tidal phase angles estimated using each of the tidal indices for the 661 analyzed events. For each tidal index except $\Delta\tau$, the distribution peak was near a tidal phase angle of

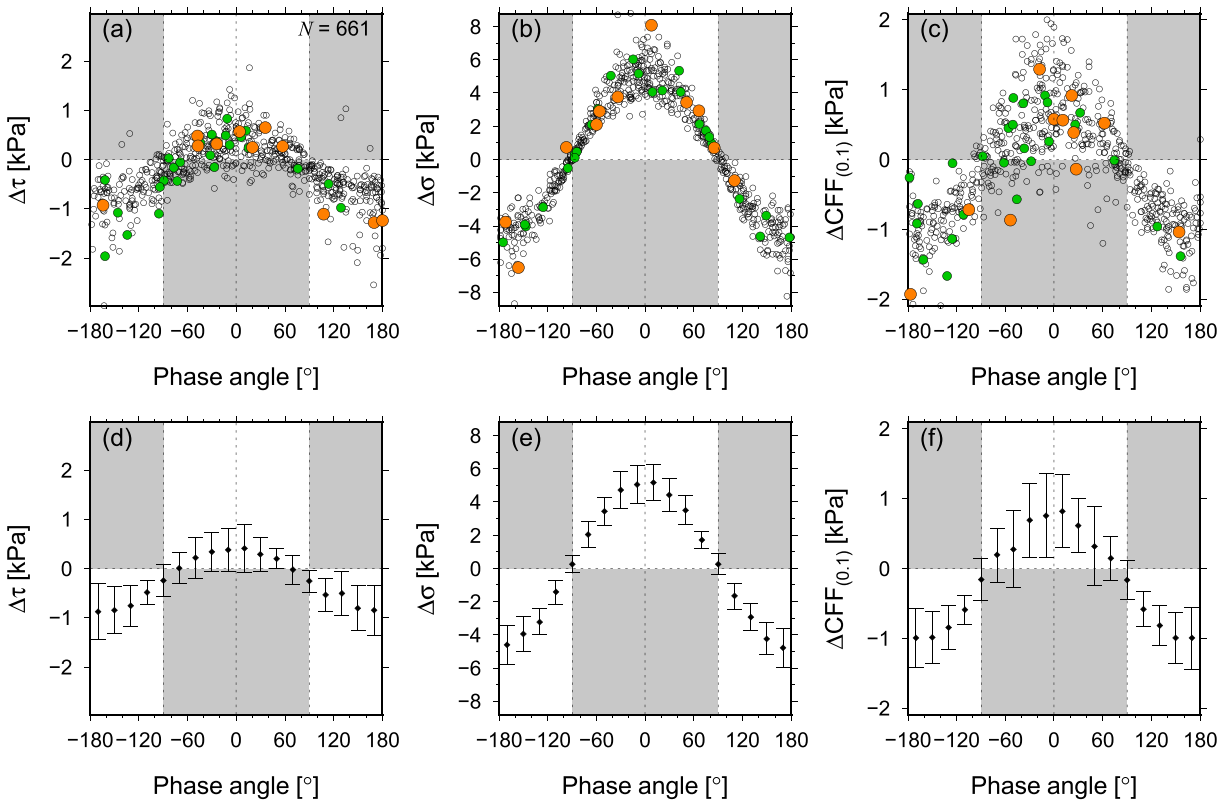


Figure 9. Relations between phase angles and tidal index levels: (a and d) shear stress $\Delta\tau$, (b and e) normal stress $\Delta\sigma$, and (c and f) $\Delta\text{CFF}_{(0.1)}$ with $\mu' = 0.1$. Orange, green, and open circles indicate events with $M_w \geq 7.0$, $M_w 6.0\text{--}6.9$, and $M_w 5.5\text{--}5.9$, respectively. Diamonds and bars in (d)–(f) denote the mean and the standard deviation, respectively.

0° ; this result indicates that earthquakes tended to occur when the tidal index level reached a local maximum. The p values of the tidal indices, which were less than 4% (except that for $\Delta\text{CFF}_{(0.1)}$), indicate the tidal triggering of earthquakes. However, care must be taken in interpreting the p value of $\Delta\tau$, as mentioned in section 3. Although $\Delta\tau$ seems to be closely related to seismicity as its p value is the smallest among the tidal indices (1.76%), the frequency distribution of the tidal phase angle has a second peak at -80 to -100° (Figure 10b). Most of the earthquakes in this interval (-80 to -100°) occurred when the tidal force acted to suppress fault slip ($\Delta\tau$ was negative), which is physically inconsistent with seismicity. Therefore, we consider not only $\Delta\text{CFF}_{(0.1)}$ but also $\Delta\tau$ to have no significant role in the tidal triggering of earthquakes, despite the apparent high correlation of $\Delta\tau$ with seismicity.

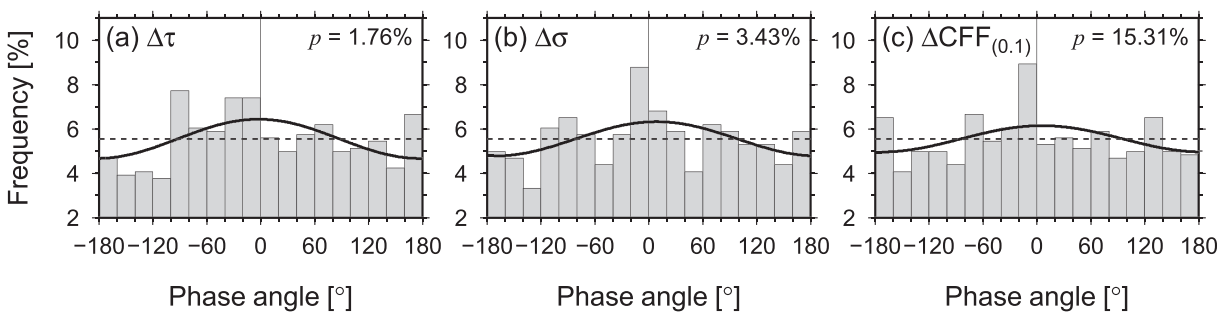


Figure 10. Frequency distributions of tidal phase angles estimated using (a) shear stress $\Delta\tau$, (b) normal stress $\Delta\sigma$, and (c) $\Delta\text{CFF}_{(0.1)}$ with $\mu' = 0.1$. The estimated p value (equation (1)) is shown in each panel. The broken horizontal line in each panel represents the mean frequency (100%/18). Solid curves represent sinusoidal functions fitted to the frequency distributions.

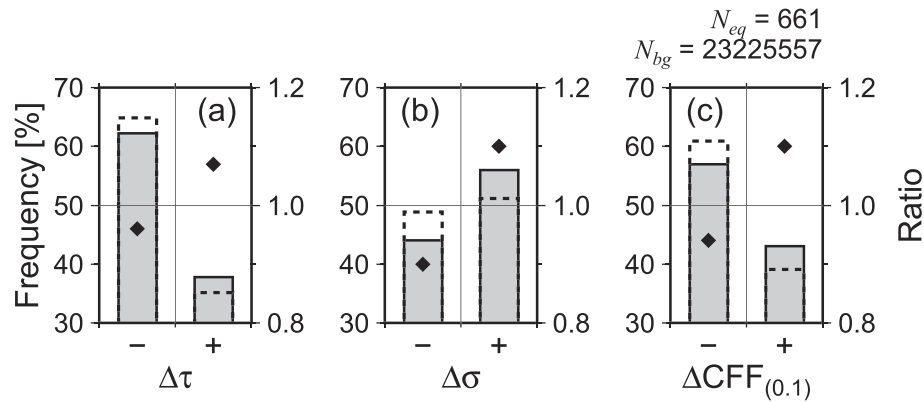


Figure 11. Frequency distribution of tidal index levels for (a) shear stress $\Delta\tau$, (b) normal stress $\Delta\sigma$, and (c) ΔCFF with $\mu' = 0.1$. Gray bars indicate frequencies of the tidal index level at earthquake occurrence times. Broken bars indicate frequencies of the background tidal index level at 15-min intervals during the 183 days before and after each earthquake (N_{bg} ; top right). Diamonds indicate ratios of these two frequencies (i.e., the gray to broken bars) for positive and negative levels.

5.2. Characteristics of Tidal Stress Levels

Here, we introduce the characteristics of the tidal stress levels. Gray bars in Figure 11 show the frequency distribution of tidal stress levels at earthquake occurrence times. Earthquakes occurred frequently at positive $\Delta\sigma$ (when tidal stress promotes fault slip) and negative $\Delta\tau$ and $\Delta CFF_{(0.1)}$ (when tidal stress suppresses fault slip). Note that the frequency distribution of positive and negative of background tidal levels is not always the same such as $\Delta\tau$ (red) in Figure 7e and $\Delta CFF_{(0.1)}$ (orange) in Figure 7f. If earthquakes occur independently in the sign of the tidal stress level, the difference between tidal stress level frequencies at earthquake occurrence times and background tidal level frequencies become small. Therefore, we compared the frequency distribution of tidal stress levels at earthquake occurrence times (Figure 11, gray bars) with the background level frequency distribution (broken bars). The latter was calculated from the tidal index levels sampled every 15 min during the 183 days before and after each earthquake (in total 23,225,557 data points). The correlation between the tidal index and earthquake occurrence can exist when the two bars are distinct. Diamonds in Figure 11 indicate ratios of these two frequencies. We found that earthquakes tended to occur selectively when the sign of the tidal index level was positive. To evaluate the significance of the difference between the tidal index level frequencies at event occurrence times and background tidal level frequencies, we tested the null hypothesis that earthquakes occur randomly with respect to the sign of the tidal level by using the chi-square test with one degree of freedom. The resulting chi-square values, 2.00 for $\Delta\tau$, 6.24 for $\Delta\sigma$, and 4.22 for $\Delta CFF_{(0.1)}$, indicate that earthquakes occur selectively depending on the sign of the tidal level because the null hypothesis was rejected at a significance level of 5% for $\Delta\sigma$ and $\Delta CFF_{(0.1)}$. As for $\Delta\tau$ however, null hypothesis could not be rejected even at a significance level of 10%.

Figure 12 shows the same as Figure 11 but abscissa is divided into 10 equal bins. Although the ratios scattered to some extent, the regression lines positively sloped. The selectivity of earthquake occurrence was prominent when the absolute values of the tidal indices level were large (Figure 12, diamonds), again except $\Delta\tau$. The tidal suppression effect was small for large negative values of $\Delta\tau$ (Figure 12a). We also conducted the same chi-square test as above but with nine degrees of freedom for Figure 12. Chi-square values became 2.98 for $\Delta\tau$, 19.25 for $\Delta\sigma$, and 15.28 for $\Delta CFF_{(0.1)}$. The result indicates that earthquakes occur selectively depending on the tidal level for $\Delta\sigma$ because the null hypothesis (earthquakes occur randomly) was rejected at a significance level of 5% (even 2.5%). As for $\Delta\tau$ and $\Delta CFF_{(0.1)}$, however, null hypothesis could not be rejected at a significance level of 5% (note that for $\Delta CFF_{(0.1)}$, null hypothesis was rejected at a significance level of 10%). Therefore, we inferred that the influence of $\Delta\tau$ on the tidal triggering of interplate earthquakes in our study area was smaller than that of the other tidal components.

Tanaka et al. (2002a) found a high correlation between $\Delta\tau$ and the occurrence of shallow, reverse fault-type earthquakes with $M_w < 7.0$ all over the world. On the other hand, we found that interplate type earthquakes along the Tonga-Kermadec trench correlated with $\Delta\sigma$ rather than $\Delta\tau$, which is consistent with the result of Tanaka et al. (2002b). Accordingly, our result and previous studies indicate that there may be regionality which of $\Delta\sigma$ and $\Delta\tau$ influence the triggering of earthquakes.

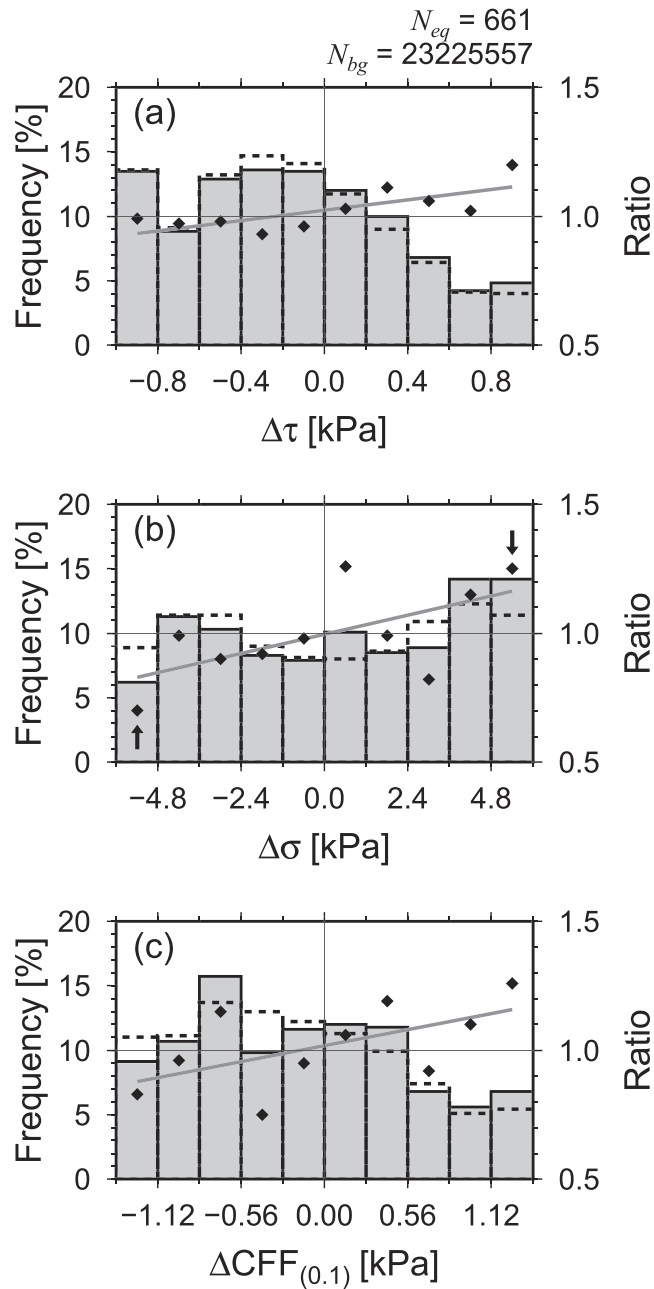


Figure 12. Same as Figure 11 but abscissa is divided into 10 equal bins. Solid and broken bars denote frequencies (%) of tidal indices level at the time of earthquake occurrence and background, respectively. Diamonds denote their relative ratio (at the time of earthquake occurrence/background). The straight gray line indicates the linear regression fit to the diamonds. We closely examined seismicity when $\Delta\sigma$ was <-4.8 or >4.8 kPa (arrows in (b)); see section 5.5.2 for details.

5.3. Relationship With the Gutenberg-Richter Law b Values

For each tidal index, we divided earthquakes into two groups according to whether the tidal index level was positive or negative when they occurred, and estimated the Gutenberg-Richter law b values (Gutenberg & Richter, 1944) for each group (Figure 13). The b value when the indices were positive was smaller than that when they were negative. In particular, we can see a difference more than the standard deviation in $\Delta\tau$ and $\Delta\sigma$. Here, we conducted strictly a significance test of the difference in b value between two groups of earthquakes using equation (33) of Utsu (1999) as follows:

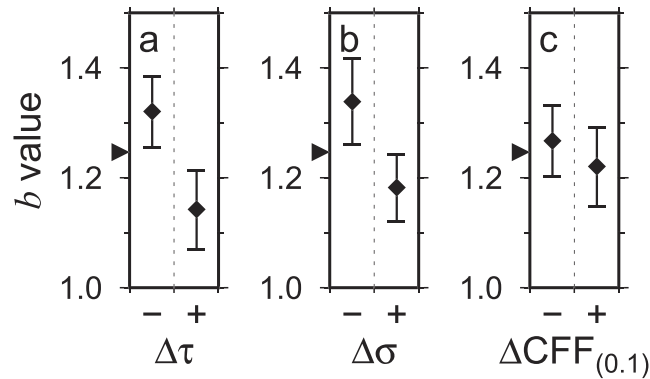


Figure 13. Estimated b values for (a) shear stress $\Delta\tau$, (b) normal stress $\Delta\sigma$, and (c) $\Delta\text{CFF}_{(0.1)}$ with $\mu' = 0.1$. The diamonds and bars show b values and their standard deviations of earthquakes occurring during periods when the tidal index level was (left) negative and (right) positive. The triangle on the left side of each panel indicates the b value estimated using all 661 events.

$$\Delta\text{AIC} = -2(N_1 + N_2)\ln(N_1 + N_2) + 2N_1\ln\left(N_1 + N_2\frac{b_1}{b_2}\right) + 2N_2\ln\left(N_1\frac{b_2}{b_1} + N_2\right) - 2, \quad (3)$$

where N_1 and N_2 are the number of earthquakes in each group and b_1 and b_2 are the maximum likelihood estimate of b in each group. If $\Delta\text{AIC} > 2$, the difference is significant. If $\Delta\text{AIC} > 5$, the difference is highly significant. We obtained the result that $\Delta\text{AIC} < 2$ for all the three components shown in Figure 13. More specifically, we obtained $\Delta\text{AIC} = 1.30$ for $\Delta\tau$ ($N_1 = 411$, $b_1 = 1.320$, $N_2 = 250$, $b_2 = 1.142$), $\Delta\text{AIC} = 0.49$ for $\Delta\sigma$ ($N_1 = 291$, $b_1 = 1.338$, $N_2 = 370$, $b_2 = 1.182$), and $\Delta\text{AIC} = -1.77$ for $\Delta\text{CFF}_{(0.1)}$ ($N_1 = 377$, $b_1 = 1.267$, $N_2 = 284$, $b_2 = 1.220$). Therefore, we conclude that the b values of the two groups do not differ significantly for all the three components.

Schorlemmer et al. (2005) showed that the global average b value is 0.9 for reverse-type faults (rake angle: 45–135°), 1.0 for strike-slip-type faults, and 1.2 for normal-type faults. The b value (1.246; Figure 1e) of inter-plate seismicity along the Tonga-Kermadec trench is larger than the global average for reverse faults (0.9), although the conditions (study period and area, fault depth, and rake angle) considered by Schorlemmer

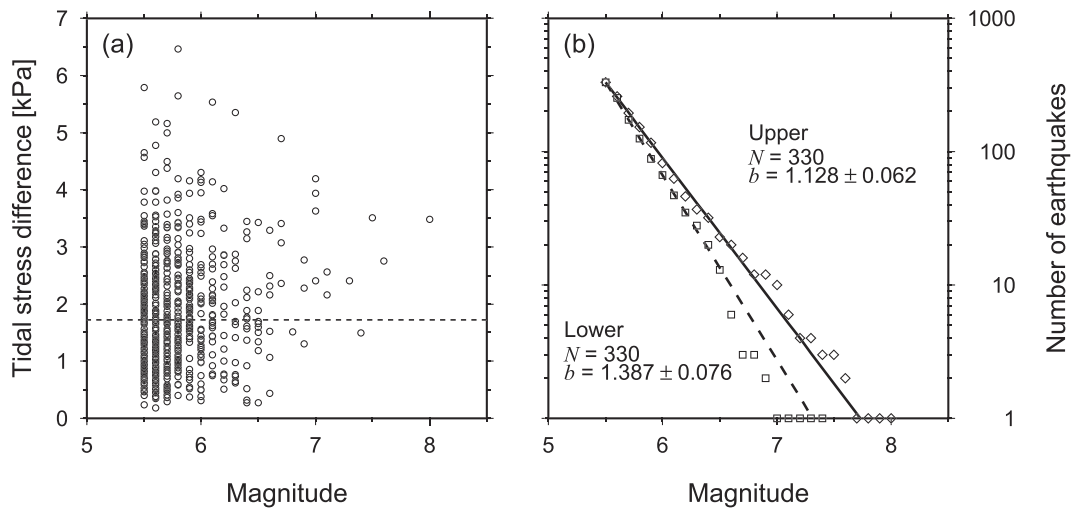


Figure 14. (a) Relation between the tidal stress differences (difference between the maximum and minimum principal stresses) at earthquake occurrence times and earthquake magnitude. The horizontal broken line indicates the median stress difference value estimated using all 661 events. (b) Cumulative magnitude frequency distributions for events with tidal stress differences higher (diamonds) and lower (squares) than the median value. The lines were drawn by fitting the Gutenberg-Richter law to the distributions.

et al. (2005) differ from those of this study. Because the b value is inversely proportional to the differential stress (i.e., the difference between the maximum and minimum principal stresses; Scholz, 2015), the relatively large b value implies that the differential stress of earthquakes in this study area may be smaller than the global average. Therefore, we next divided earthquakes into two groups according to whether the tidal stress difference was higher or lower than the median value of all 661 analyzed earthquakes, and estimated the b value for each group (Figure 14). The b value of the higher stress difference group tended to be smaller than that of the lower group, consistent with the results of rock deformation experiments (Scholz, 1968). Here, we also conducted the significance test based on equation (3), resulting in $\Delta AIC > 5$. Therefore, we conclude that the difference in b value between two groups is highly significant. Although the variation of tidal stress was only on the order of kilopascals, tidal stress perturbations are synchronously applied to asperities over a wide area for hours, which might facilitate cascading ruptures (Noda et al., 2013) and lead to a large-magnitude rupture, resulting in a small b value. From the result of the significance test for Figure 14b, we consider that the perturbation of the differential stress may influence earthquake magnitudes (i.e., the growth of fault slips after the rupture started). Note that the correlation coefficient between earthquake magnitude and tidal stress difference was 0.14.

5.4. Information Related to Pore Pressure

For ΔCFF , we assumed $\mu' = 0.1, 0.4,$ and 0.7 to estimate the apparent friction coefficient and to obtain the information related to pore pressure at the plate boundary from the degree of tidal correlation with seismicity. Equation (A7) ($\Delta CFF = \Delta\tau + \mu' \Delta\sigma$) in Appendix A4 can be rewritten by $\Delta CFF = \Delta\tau + \mu_0(\Delta\sigma + \Delta p)$, where μ_0 and Δp represent the static friction coefficient and pore pressure, respectively. Since $\Delta p \propto -\Delta\sigma$ in mature fault zone (Cocco & Rice, 2002), we can set $\Delta p = -k\Delta\sigma$ and $\mu' = \mu_0(1 - k)$. Accordingly, if the response of pore pressure to $\Delta\sigma$ is strong (i.e., $k \sim 1$) at the plate boundary, the apparent friction coefficient is small ($\mu' \sim 0$) and the contribution of $\Delta\tau$ to ΔCFF becomes dominant. In contrast, if the response of pore pressure to $\Delta\sigma$ is weak (i.e., $k \sim 0$), the apparent friction coefficient is large ($\mu' \sim \mu_0$) and the contribution of $\Delta\sigma$ whose amplitudes are naturally about 5–10 times of those of $\Delta\tau$ to ΔCFF becomes dominant. As mentioned above, we found a correlation of tidal triggering of earthquakes with $\Delta\sigma$ rather than with $\Delta\tau$ and $\Delta CFF_{(0.1)}$. Therefore, we infer that the apparent friction coefficient is relatively large at the plate boundary along the Tonga-Kermadec trench rather than other areas, and this can be attributed to the weak response of pore pressure to $\Delta\sigma$. No slow earthquakes that tend to occur in the environment of high pore fluid pressure have been reported yet along the Tonga-Kermadec trench (Obara & Kato, 2016), supporting the influence of pore pressure may be weak there.

5.5. Relation With Tectonic Setting

5.5.1. Background Tectonics

Both the plate convergence rate and background seismicity along the trench increase from south to north (Ide, 2013), and the bending angle of the subducting slab decreases southward. In this regard, Nishikawa and Ide (2015) have pointed out that the background seismicity rate in subduction zones is related to hydration associated with slab bending. Note that the number of interplate type earthquakes that we extracted increase southward (Figure 1c), although we do not separate them in background seismicity and aftershocks (see section 5.5.2).

The Lau Basin (LB in Figure 15a), near the northern end of the Tonga trench, is spreading in an east-west direction at a rate of 6.5–10 cm/year, similar to mid-ocean ridges (Fujiwara et al., 2001; Taylor et al., 1996; Turner & Hawkesworth, 1998). The Havre trough (HT in Figure 15a), which is located to the south of the Lau Basin, is rifting in the east-west direction at 6 cm/year (Parson & Wright, 1996). The Louisville seamount chain lies to the east of the Kermadec trench and is aligned NNW-SSE (Figure 15a). The collision zone between the Louisville seamount chain and the trench has migrated $\sim 1,000$ km ($\sim 10^\circ$ of latitude) southward at a rate of 18 cm/year over the past 5 Myr (Ballance et al., 1989). Their continuous collision is causing the Tonga trench to shift westward (Lallemant et al., 1992). According to Scholz and Small (1997), subduction of a large seamount generally increases the normal stress across the subduction interface, thereby strengthening seismic coupling and increasing earthquake recurrence intervals. However, it has also been claimed that the passage of a subducted seamount promotes stable sliding (e.g., Mochizuki et al., 2008). Although these two interpretations are mutually exclusive, either can cause low seismicity, and, in fact, seismicity is low at 18.6°S around the Capricorn Seamount, at 25.7°S around the subducting Mo'unga Seamount of the

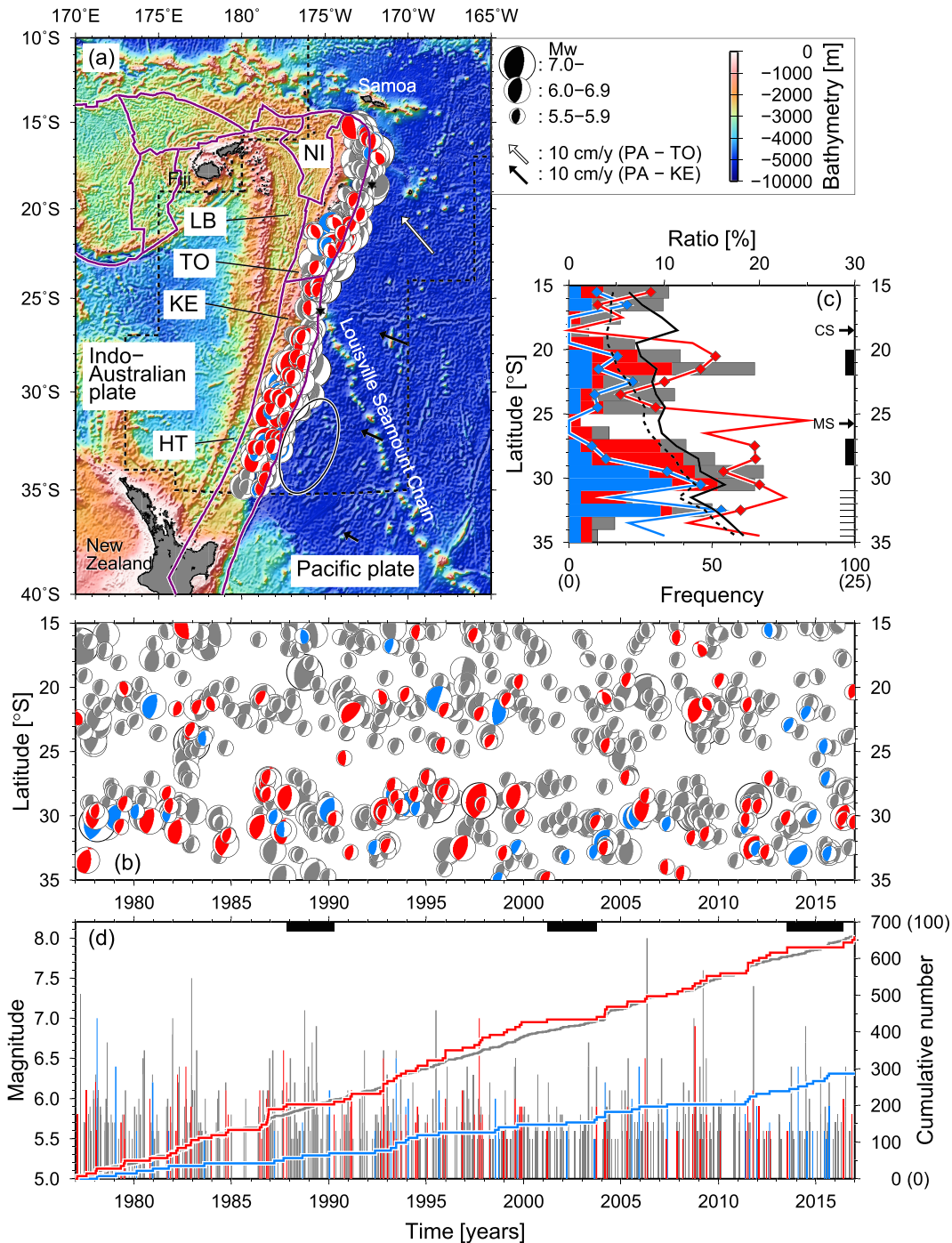


Figure 15. (a, b, and d) Same as Figure 1a, 1b, and 1d, except red and blue symbols indicate events that occurred when $\Delta\sigma > 4.8$ kPa and $\Delta\sigma < -4.8$ kPa, respectively, and focal mechanism solutions are taken from the GCMT catalog (Dziewonski et al., 1981; Ekström et al., 2012). NI, LB, and HT denote the Niufo'ou plate, Lau basin, and Havre trough, respectively. (c) Frequencies of earthquakes that occurred when $\Delta\sigma > 4.8$ kPa (red columns) and $\Delta\sigma < -4.8$ kPa (blue columns) per degree of latitude. The gray columns denote the total number of earthquakes per degree of latitude. On the lower horizontal axis, the frequencies in parentheses are for events that occurred when $\Delta\sigma > 4.8$ kPa or $\Delta\sigma < -4.8$ kPa. The relative frequency ratios of earthquake occurrence when $\Delta\sigma > 4.8$ kPa or $\Delta\sigma < -4.8$ kPa to the total number of events are shown by red and blue lines, respectively, and diamonds indicate the ratios when the total number of events (gray columns) was 30 or more. The solid and broken black lines indicate the relative frequency ratios of $\Delta\sigma > 4.8$ kPa and $\Delta\sigma < -4.8$ kPa, respectively, to the background tidal index level variation evaluated every 15 min during the 183 days before and after each earthquake. The two thick bars on the right side indicate latitudes where the relative frequency ratio of earthquakes that occurred when $\Delta\sigma > 4.8$ kPa or $\Delta\sigma < -4.8$ kPa (red/blue diamonds) was significantly larger or smaller, respectively, than the frequency ratio relative to the background variation (solid/broken black lines). In these areas, we considered earthquake triggering to be controlled by $\Delta\sigma$. The thin bars at the bottom right represent seamounts on the outer rise. In (d), the cumulative numbers in parentheses on the right-side axis are for events that occurred when $\Delta\sigma > 4.8$ kPa or $\Delta\sigma < -4.8$ kPa, and the three thick bars at the top indicate periods of earthquake quiescence when $\Delta\sigma > 4.8$ kPa.

Louisville seamount chain and at 31–35°S a cluster of petite seamounts on the outer rise (Figure 1c). In addition, the behavior of subducting seamounts differs between Chilean- and Marianas-type convergent margins (Cloos & Shreve, 1996). Tonga trench and Kermadec trench are categorized as Marianas-type (erosion) and Chilean-type (accretion), respectively. In any case, there seems to be a close spatial relationship between the occurrence pattern of earthquakes and tectonics along the Tonga-Kermadec trench.

5.5.2. High-Sensitivity Area to $\Delta\sigma$

Next, we focused on the relationship between the tectonics and $\Delta\sigma$, which might control triggering of interplate earthquakes. The ratio of tidal index level frequencies to background tidal level frequencies was relatively large for $\Delta\sigma > 4.8$ kPa and small for $\Delta\sigma < -4.8$ kPa (Figure 12b, arrows). We compared the spatiotemporal distribution between 94 events that occurred when $\Delta\sigma > 4.8$ kPa (Figure 15, red symbols) and 41 events that occurred when $\Delta\sigma < -4.8$ kPa (blue symbols). We also estimated the occurrence frequency ratio per degree of latitude for earthquakes that occurred when $|\Delta\sigma| > 4.8$ kPa relative to all 661 analyzed earthquakes (Figure 15c). The relative frequency ratios (%) of background tidal levels for both $\Delta\sigma > 4.8$ kPa (solid black line) and $\Delta\sigma < -4.8$ kPa (broken black line) become larger southward. We located four virtual faults with fault parameters (depth: 15 km, strike: 200°, dip: 25°, and rake: 95°) derived by averaging those of the 661 events (see Figure 3) along the trench at equal latitudinal intervals from the north (172.5°W, 17.5°S) to the south (178.0°W, 32.5°S), and then we calculated theoretical tidal indices variation. As a result, tidal stress level of $\Delta\sigma$ tended to become bigger southward. This result may indicate a possible reason of higher interplate seismicity in the southward area. Broadly speaking, the frequencies of events occurring when $\Delta\sigma > 4.8$ kPa (red line) and $\Delta\sigma < -4.8$ kPa (blue line) also tended to increase southward. Even so, in the latitudinal ranges 20–22°S and 27–29°S (thick bars on the right side in Figure 15c), the relative frequency ratios of earthquakes that occurred when $\Delta\sigma > 4.8$ (red lines) and $\Delta\sigma < -4.8$ kPa (blue lines) were significantly larger and smaller, respectively, than the corresponding relative frequency ratios of background level variations. These two areas, which are particularly sensitive to $\Delta\sigma$, are away from the subducting Capricorn and Mo'unga seamounts and from a cluster of petite seamounts on the outer rise; therefore, roughness at the plate boundary might be low in these areas. The high sensitivity of seismicity to $\Delta\sigma$ in these areas is consistent with a high apparent friction coefficient and low plate interface roughness. On the other hand, because the subduction of seamounts increases normal stress across a plate interface (Scholz & Small, 1997), in areas where seamounts are subducting, the influence of $\Delta\sigma$ on seismicity, and hence the tidal dependency of seismicity, might be relatively small. This result does not deny that the passage of a subducted seamount promotes stable sliding. We cannot judge it because no earthquake occurs in stable sliding area. A future supplemental study is necessary to clarify the above speculation.

5.6. Periodic Variations of Seismicity

When $\Delta\sigma > 4.8$ kPa (red symbol in Figure 15), seismicity seemed to display periodic quiescence (thick bars at the top of Figure 15d). When seismicity satisfies the homogeneous Poisson process with the average occurrence rate of ν , the number of earthquakes during a time interval of Δt obeys the Poisson distribution with the expectancy of $\nu\Delta t$. Using this property, we can estimate degrees of temporal seismic quiescence and activation during a specific time interval. Firstly, we carried out the declustering procedure. An event was linked to others together under the condition that the epicenter distance was within 30 km and the occurrence time difference was within 30 days, and then the cluster was represented by an event with the largest magnitude. By this declustering procedure, the number of events was decreased from 661 to 533. We confirmed that the null hypothesis, earthquakes occur under homogeneous Poisson process, was not rejected at a significance level of 5%. Among 94 events that occurred when $\Delta\sigma > 4.8$ kPa, 69 events corresponded to the declustered catalog obtained by the above procedure. We defined a seismicity index to detect periods of active and quiescent seismicity. We assumed seismicity to be a homogeneous Poisson process, and established seven seismicity index categories (−3, −2, −1, 0, 1, 2, and 3) such that the probability of a certain number of earthquakes occurring within each time window is 5%, 10%, 15%, 40%, 15%, 10%, and 5%, respectively, and we assumed a mean seismicity rate of 69 events in 40 years. Seismicity index values of 3 and −3 indicate significantly high activity and significant quiescence, respectively. We calculated the seismicity index every 180 days (approximately half a year) within a 1,080-day (approximately three-year) temporal window (Figure 16). Seismicity index 3 corresponds to the number of nine or more, and −3 corresponds to less than one, according to the mean seismicity rate of 5.10 events in 1,080 days. The result shows not only periodic quiescence (around 1989, 2002, and 2015) but also periodic activation (around 1982, 1997, and 2008) with the period of over

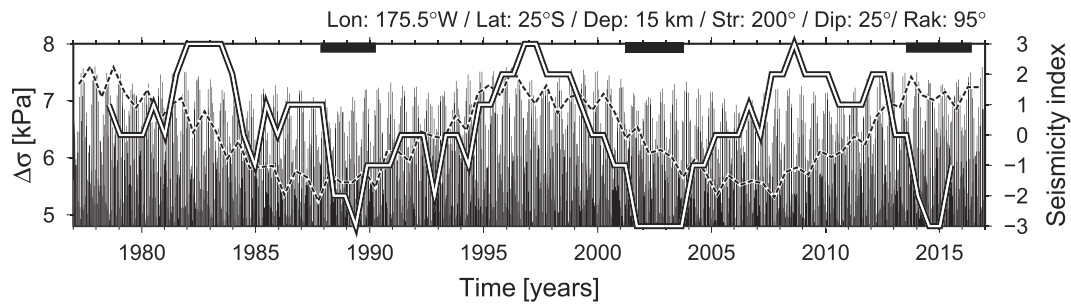


Figure 16. Example of background variation of $\Delta\sigma$ over 40 years (nearly vertical black lines), based on the assumed fault parameters shown above the graph (see Figure 3). The double line shows seismicity index values (see section 5.6 for details). The broken line indicates the relative frequency of the tidal background variation when $\Delta\sigma > 4.8$ kPa, calculated at six-month intervals, and corresponds to the 18.61-year tidal cycle. The three thick bars at the top is the same as those in Figure 15.

10 years appeared alternately. The long-term variation in seismicity, however, does not correspond to the well-known long-term tidal cycles, which have periods of 8.85 and 18.61 years. Figure 16 also shows the 40-year variation of $\Delta\sigma$ based on assumed fault parameters derived by averaging those of the 661 events (see Figure 3). Note that although the amplitude and phase of $\Delta\sigma$ depend to some extent on the assumed fault parameters, they do not affect the long-term trend in $\Delta\sigma$. As a result, we were unable to identify any sensitivity of seismically active or quiescent periods to $\Delta\sigma > 4.8$ kPa.

We also calculated the seismicity indices for earthquakes which occurred at $\Delta\tau > 0.8$ kPa and $\Delta\text{CFF}_{(0.1)} > 1.12$ kPa according to Figure 12. Although the fluctuation of seismicity for positive $\Delta\tau$ and $\Delta\text{CFF}_{(0.1)}$ also appeared, we could not find the clear periodicity of them.

Uchida et al. (2016) found periodic seismicity in northeastern Japan using repeating earthquakes and Global Navigation Satellite System, indicating periodic plate motion fluctuation. Their result is similar to periodic quiescence and activation shown in Figure 16 although the periods are different: a few years in the Japan and over 10 years in our study area. As both regions are located in the convergence area of the Pacific Plate, existence of periodic plate motion fluctuation in this studied region would not be unlikely. The effect of $\Delta\sigma$ would become relatively small when the plate motion rate (tectonic loading rate) is high. Thus, earthquakes tend to occur even if the perturbation associated with tide is small. Accordingly, seismic quiescence may appear because the number of earthquakes satisfying the condition of $\Delta\sigma > 4.8$ kPa decreases. This topic should be examined by a future supplemental study after the accumulation of more seismic data.

6. Summary

We investigated spatiotemporal variations in the relation between the Earth tide and the occurrence of interplate type events with $M_w \geq 5.5$ along the Tonga-Kermadec trench during 1977–2016. We considered the tidal responses of volumetric strain (ΔV), shear stress ($\Delta\tau$), normal stress ($\Delta\sigma$), and the Coulomb failure function (ΔCFF ; calculated assuming values of 0.1, 0.4, and 0.7 for the apparent friction coefficient), and closely examined not only the tidal phase angle but also the tidal index levels themselves. We found a correlation of seismicity with $\Delta\sigma$ rather than with $\Delta\tau$, and earthquakes tended to occur when the tidal force promoted fault slip. The selectivity of earthquake occurrence is more noticeable when absolute tidal index levels are larger; that is, earthquakes tend to occur when the tidal indices have large positive values and tend to be suppressed when large negative values. Our results also suggest that the apparent friction coefficient is relatively large at the plate boundary along the Tonga-Kermadec trench, which implies that the response of pore pressure to $\Delta\sigma$ is weak. At around 20–22°S and 27–29°S, seismicity is particularly sensitive to $\Delta\sigma$. The b values of the Gutenberg-Richter relation decrease when the tidal stress difference (difference between the maximum and minimum principal stresses) is high, consistent with the results of rock deformation experiments.

This study confirmed the tidal triggering of earthquakes and identified areas sensitive to tidal stress along the Tonga-Kermadec trench. We hope that this information will be of some use in earthquake forecasting.

Appendix A.

A1. Theoretical Tidal Stress

A1.1. Solid Tide

To calculate solid tides, we developed a program that combined the formulations of six independent strain tensor components described by Ozawa (1974) with the tide-generating potential time series calculation logic of Nakai (1979). This program reads the eigenfunctions (see section A2.) of the solid tide (spherical wave number = 2) calculated for a static case and calculates time series for the six strain tensor components at an arbitrary depth. Note that we corrected a mistake in Ozawa (1974) so that the tide-generating potential was not differentiated in the radial direction when strain components including radial differentiation were calculated.

Although the GOTIC2 program (Matsumoto et al., 2001) can calculate the solid tide, it does so at the Earth's surface, where the shear strain is zero owing to the free surface boundary condition, which does not hold at depth. Furthermore, GOTIC2 incorporates no more than 21 tidal constituents. Because the contribution of the solid tide to the total Earth tide is large, we instead used our program, which achieves greater accuracy by multiplying the tide-generating potential, calculated directly from the celestial coordinates of the Sun and Moon, by eigenfunctions (see section A2).

A1.2. Ocean Loading

The elastic response of the solid Earth to ocean tide loading is obtained by the convolution of Green's functions (see section A3) for the surface vertical point loading with the loading mass distribution, which is given in terms of spherical ocean tide models for each of the 21 constituents.

We used the ocean tide model NAO.99b (Matsumoto et al., 2000) for the 16 major constituents in short-period bands (M2, S2, K1, O1, N2, P1, K2, Q1, M1, J1, OO1, 2N2, Mu2, Nu2, L2, T2) and model NAO.99L (Takanezawa et al., 2001) for the five constituents in long-period bands (Mtm, Mf, Mm, Ssa, Sa). We divided the ocean regions into cells of size $0.5^\circ \times 0.5^\circ$ (first mesh) for $\Theta > 10^\circ$, $5' \times 5'$ (second mesh) for $5^\circ < \Theta \leq 10^\circ$, $30'' \times 30''$ (third mesh) for $0.2^\circ < \Theta \leq 5^\circ$, and $1.5'' \times 1.5''$ (fourth mesh) for $\Theta \leq 0.2^\circ$, where Θ is the angular distance from the loading point. If land was present in the cell, only the proportion of ocean area within the cell was considered. For epicenters in and around Japan, the ocean tide model NAO.99Jb (Matsumoto et al., 2000) replaced NAO.99b for the 16 major constituents. For hypocenters in and around Japan, mesh sizes of $7.5' \times 5'$ for $5^\circ < \Theta \leq 10^\circ$, $45'' \times 30''$ for $0.2^\circ < \Theta \leq 5^\circ$, and $2.25'' \times 1.5''$ for $\Theta \leq 0.2^\circ$ were used, in accordance with GOTIC2.

For several reasons, we needed to modify GOTIC2 to calculate the ocean tide loading effect. GOTIC2 cannot model deformation beneath the seafloor because it uses only Green's functions for deformation at the surface. GOTIC2 also assumes that the point of interest (usually a crustal deformation observatory) is on land, which was not the case for the oceanic hypocenters in this study. Finally, when calculating the contribution from oceanic cells, GOTIC2 assumes that the shortest distance from the point of interest to the cell is greater than 0.0001° , because its Green's functions are not applicable to angular distances less than 0.0001° ($0.36''$) and it is not proper to extrapolate to smaller distances (see section A3). Therefore, it is not possible to calculate the contribution from the cell that includes the epicenter, or from cells whose shortest distance to the epicenter is less than 0.0001° . Therefore, in this study, we excluded these cells of the fourth mesh from the calculation. The maximum total area of the excluded cells was $3.0'' \times 3.0''$ (or $4.5'' \times 3.0''$ in and around Japan), corresponding to a surface area of about $100 \text{ m} \times 100 \text{ m}$. If the hypocenter was deeper than 1 km, the contributions from these cells were disregarded (see section A5). Had there been any hypocenters shallower than 1 km, it would have been necessary to evaluate their contribution by using the Boussinesq approximation, but there were no such hypocenters in this study.

The behavior of Green's functions underground in the vicinity of the loading point becomes complicated (see section A3). In GOTIC2, contributions from each oceanic cell are evaluated analytically by approximating the Green's functions within a cell with a quadratic function. For suitable accuracy, this approximation requires a small cell size, even in areas where the ocean is widely distributed. Therefore, in this study, we used the MESH4 and FULLMESH options of GOTIC2 for all events. Note that volumetric strain ϵ_{vol} was evaluated by numerical integration, because it includes a term for which no analytical expression of integration exists.

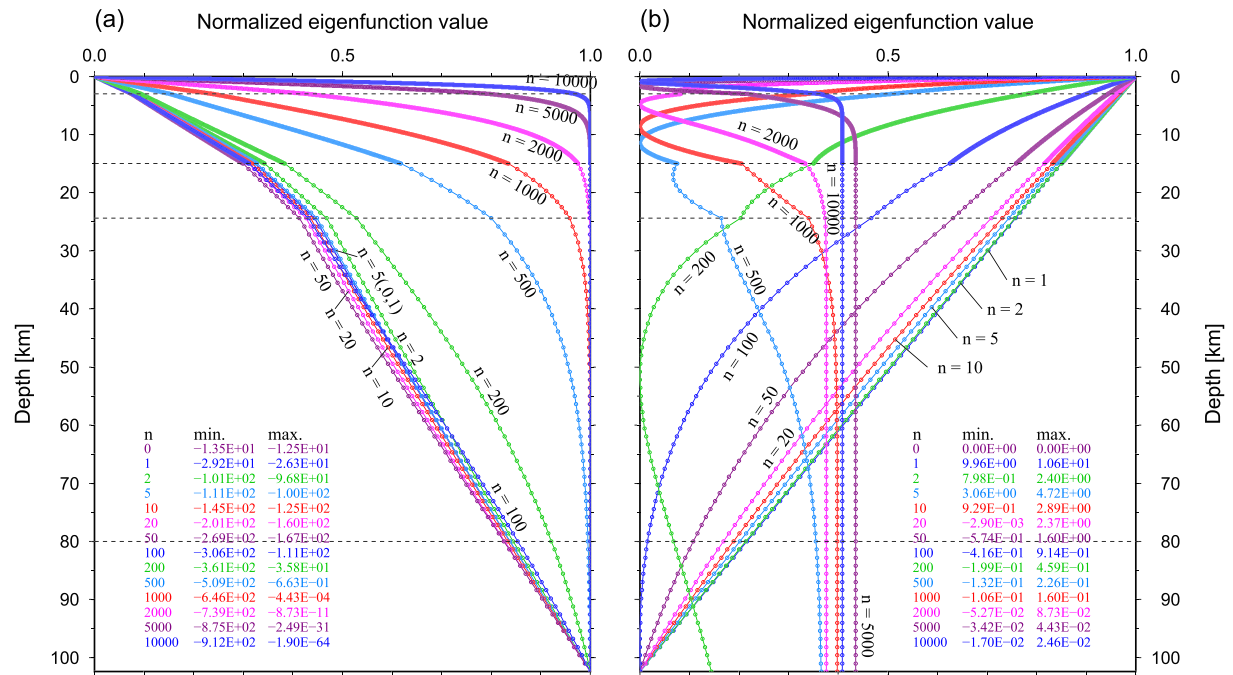


Figure A1. Depth profiles of eigenfunctions (a) $y_1^i(r)$ and (b) $y_3^i(r)$ for different spherical wave numbers n (colored lines) calculated using PREM. The normalized eigenfunction value is shown on the abscissa; see Appendix A2 for details. Wave numbers and the corresponding minimum and maximum values [km/(km/s)²] are listed within each plot. The spacing of dots on the profile lines represents the grid intervals.

A2. Eigenfunctions

We followed Kamigaichi (1998) in calculating the eigenfunctions $y_i^i(r)$ ($i = 1, 2, \dots, 6$) of the Earth for a static case. However, we changed the Earth model from 1066A (Gilbert & Dziewonski, 1975) to PREM (Dziewonski & Anderson, 1981) with the following slight modification: the top 3-km layer was replaced by a solid layer following Tsuruoka et al. (1995) ($V_p = 5$ km/s, $V_s = 2.6$ km/s, $\rho = 2.6$ g/cm³). When calculating eigenfunctions for the solid tide, which has a very long wavelength, it is not necessary to set the integration grid interval as fine as when calculating eigenfunctions for surface vertical loading, but a very fine grid interval is necessary to calculate the Green's functions for the eigenfunctions for surface vertical loading. We set grid intervals according to the spherical wave number n and the layer boundaries in the Earth model for the depth range 0–102.4 km and $n \leq 5,000$ as follows: 0.0075 km (400 grid cells deep) for 0.0–3.0-km depth, 0.006 km (2,000 cells deep) for 3.0–15.0-km depth, 0.94 km (10 cells deep) for 15.0–24.4-km depth, 1.39 km (40 cells deep) for 24.4–80.0-km depth, and 1.4 km (16 cells deep) for 80–102.4-km depth. For $n > 5,000$, we used a 75-cm (0.00075 km) grid interval (4,000 cells deep) in the uppermost layer (0.0–3.0-km depth) to secure sufficient accuracy. In this study, we set the upper limit of n to 10,000. Higher values of n would be necessary for hypocenters shallower than 10 km (Kamigaichi, 1998), but no such hypocenters were targets in this study. In calculation of the theoretical tidal response just at the depth of the physical property boundary in the Earth model, our calculation program uses the physical property in the upper layer.

Green's functions were calculated by eigenfunctions $y_1^i(r)$ and $y_3^i(r)$ and their respective spatial differentiations ($\frac{dy_1^i(r)}{dr}$, $\frac{dy_3^i(r)}{dr}$; see section A3). Figure A1 shows the depth profiles of these eigenfunctions for surface vertical loading for various values of n . The function values are normalized by $\frac{dy_i^i(r) - \min_i^i}{\max_i^i - \min_i^i}$ for any n , where \min_i^i and \max_i^i are the minimum and maximum values for each n and i , respectively. The general appearance of $y_1^i(r)$ in Figure A1a is similar to that in Figure 1 of Kamigaichi (1998), where the eigenfunction is normalized by the surface value. The absolute values of these eigenfunctions have their maximum at the surface for any n and decrease monotonically with depth. For higher n , the deformation is limited to the shallowest crust, and the eigenfunction values are mainly controlled by the structure of this region. For lower n , however, the mantle as

a whole deforms and the eigenfunction values are strongly controlled by the mantle structure. The absolute values of $y_3^n(r)$ (Figure A1b) have their maximum at the surface for any n and also decay with depth. The depth at which $y_3^n(r)$ changes its sign becomes shallower with increasing n .

A3. Green's Functions

We followed the procedure of Kamigaichi (1998) when converting the eigenfunctions for surface vertical loading for various values of n to Green's functions for the surface vertical point load. The obtained Green's functions were for radial (vertical) displacement (U_r), colatitudinal (horizontal) displacement (U_θ), colatitudinal linear strain ($E_{\theta\theta}$), radial linear strain (E_{rr}), shear strain ($E_{r\theta}$), and volumetric strain (E_{vol}) in spherical coordinates (r, θ, ϕ) . Figure A2 shows the normalized angular distance profiles of these Green's functions for various depths. The number of calculation points (angular distances) in GOTIC2 is 50 (as in Table A3 of Farrell, 1972), but in this study we increased the number of calculation points to 81, of which 72 points were set to $(1.0, 1.2, 1.6, 2.0, 2.5, 3.0, 4.0, 5.0, 6.0, 7.0, 8.0, 9.0) \times 10^{(-4, -3, -2, -1, 0, 1)^\circ}$ for $\Theta < 100^\circ$ and nine points were at 10° intervals for $\Theta \geq 100^\circ$. In the original GOTIC2, the nearest angular distance from the loading point is $1.0 \times 10^{(-4)^\circ}$, which is the same as in this study, and the next nearest points are at $1.0 \times 10^{(-3)^\circ}$ and $1.0 \times 10^{(-2)^\circ}$, but this spacing is too coarse for our purposes. The plots in Figure A2, similar to Figure 3 of Kamigaichi (1998) focusing on the borehole sensor installation depth ($d < 1$ km), show the differences in the features at $\Theta \approx 0.1^\circ$ at the surface due to the different Earth models used.

We derived the six independent components of the strain tensor from the six physical quantities listed above. Formulations of E_{rr} and $E_{r\theta}$, which were not dealt with by Kamigaichi (1998), are respectively,

$$E_{rr} = \frac{G}{a} \sum_{n=0}^{\infty} \frac{dy_1^n(r)}{dr} P_n(\cos \theta), \quad (\text{A1})$$

$$E_{r\theta} = \frac{1}{2} \frac{G}{a} \sum_{n=1}^{\infty} \left(\frac{y_1^n(r)}{r} - \frac{y_3^n(r)}{r} + \frac{dy_3^n(r)}{dr} \right) \frac{\partial P_n(\cos \theta)}{\partial \theta}, \quad (\text{A2})$$

where G is the gravitational constant, a is the Earth's radius, $y_1^n(r)$ and $y_3^n(r)$ are the eigenfunctions for the n th order, and $P_n(\cos \theta)$ is the Legendre function of the n th order. Note that the components U_ϕ , $E_{r\phi}$, and $E_{\theta\phi}$ are not generated because of the symmetry of the point-loading problem, and $E_{\phi\phi}$ is nonzero, but can be obtained in terms of U_r and U_θ (Kamigaichi, 1998). It is sufficient to set the upper limit of the summation order ($n = 10,000$) to depths (≥ 10 km) where interplate earthquakes occur (Kamigaichi, 1998).

A4. Conversion to Assumed Fault Coordinates

The coordinate system used in this study defines east, north, and up as positive values of x , y , and z , respectively, in accordance with GOTIC2. We converted the data from this coordinate system to one oriented with respect to the assumed fault (x'' , slip direction; y'' , fault-normal; z'' , $x'' \times y''$) by rotating the coordinates twice. The first rotation was from the original to the coordinate system (x' north, y' east, z' down), as shown in Figure 4.20 of Aki and Richards (2002). The conversion (rotation) matrix \mathbf{A}_1 from $\{x, y, z\}$ to $\{x', y', z'\}$ is

$$\mathbf{A}_1 = \begin{pmatrix} 0 & 1 & 0 \\ 1 & 0 & 0 \\ 0 & 0 & -1 \end{pmatrix}. \quad (\text{A3})$$

The second conversion (rotation) matrix \mathbf{A}_2 from $\{x', y', z'\}$ to $\{x'', y'', z''\}$ is

$$\mathbf{A}_2 = \begin{pmatrix} \cos \lambda \cos \phi_s + \cos \delta \sin \lambda \sin \phi_s & \cos \lambda \sin \phi_s - \cos \delta \sin \lambda \cos \phi_s & -\sin \lambda \sin \delta \\ -\sin \delta \sin \phi_s & \sin \delta \cos \phi_s & -\cos \delta \\ * & * & * \end{pmatrix}, \quad (\text{A4})$$

where ϕ_s is the strike, δ is the dip angle, and λ is the rake. The third row in equation (A4) is the vector product of the first-row and second-row vectors and is abbreviated here for simplicity. The total coordinate

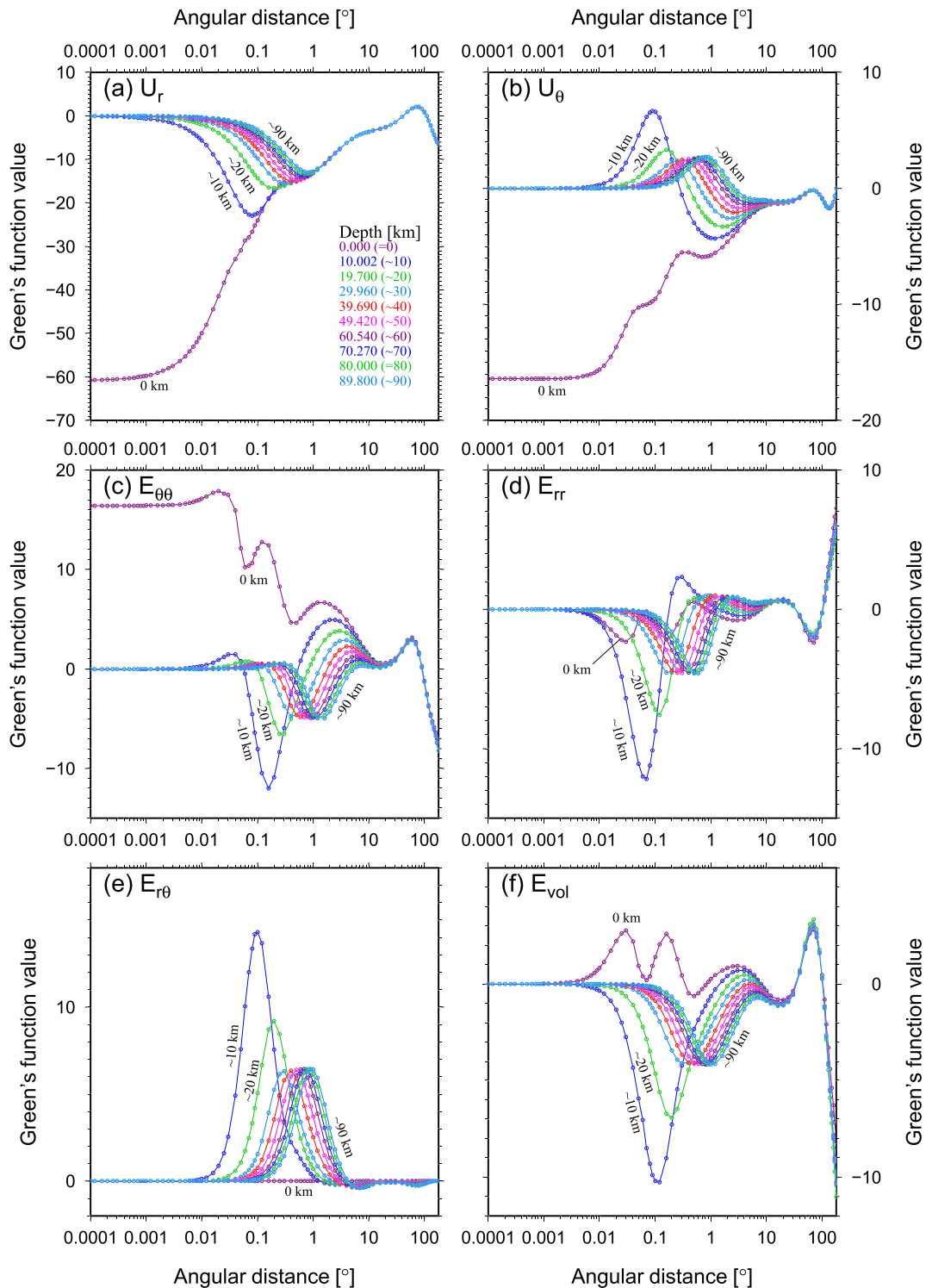


Figure A2. Angular distance profiles of Green's functions for (a) U_r , (b) U_θ , (c) $E_{\theta\theta}$, (d) E_{rr} , (e) $E_{r\theta}$, and (f) E_{vol} at various depths for a 1-kg vertical point load at the surface. Displacements are multiplied by $(a\theta) \times 10^{12}$, and strains are multiplied by $(a\theta)^2 \times 10^{12}$, where a is the Earth's radius in meters.

conversion (rotation) matrix \mathbf{A} is represented by $\mathbf{A} = \mathbf{A}_2\mathbf{A}_1$. The relation between the strain tensors in the original coordinates (\mathbf{E}) and the fault coordinate system (\mathbf{E}'') is expressed as $\mathbf{E}'' = \mathbf{A}\mathbf{E}\mathbf{A}^T$. Shear stress $\Delta\tau$, normal stress $\Delta\sigma$, and ΔCFF on the assumed fault plane are represented as

$$\Delta\tau = 2\mu_L \varepsilon_{x''y''}, \quad (\text{A5})$$

$$\Delta\sigma = \lambda_L \varepsilon_{\text{vol}} + 2\mu_L \varepsilon_{y''y''}, \quad (\text{A6})$$

$$\Delta CFF = \Delta\tau + \mu' \Delta\sigma, \quad (\text{A7})$$

where ε_{vol} is the volumetric strain and is independent of the coordinate system; λ_L and μ_L are the Lamé's coefficients obtained from $\lambda_L = \rho(V_p^2 - 2V_s^2)$ and $\mu_L = \rho V_s^2$, respectively; and μ' is the apparent friction coefficient. By using the six independent components of the strain tensor ($\varepsilon_{xx}, \varepsilon_{yy}, \varepsilon_{zz}, \varepsilon_{xy}, \varepsilon_{xz}, \varepsilon_{yz}$) obtained in the original coordinate system, $\varepsilon_{x''y''}$, $\varepsilon_{y''y''}$, and ε_{vol} are represented as follows:

$$\varepsilon_{x''y''} = a_{11}b_1 + a_{12}b_2 + a_{13}b_3, \quad (\text{A8})$$

$$\varepsilon_{y''y''} = a_{21}b_1 + a_{22}b_2 + a_{23}b_3, \quad (\text{A9})$$

$$\varepsilon_{\text{vol}} = \varepsilon_{xx} + \varepsilon_{yy} + \varepsilon_{zz}, \quad (\text{A10})$$

$$b_1 = a_{21}\varepsilon_{xx} + a_{22}\varepsilon_{xy} + a_{23}\varepsilon_{xz}, \quad (\text{A11})$$

$$b_2 = a_{21}\varepsilon_{xy} + a_{22}\varepsilon_{yy} + a_{23}\varepsilon_{yz}, \quad (\text{A12})$$

$$b_3 = a_{21}\varepsilon_{xz} + a_{22}\varepsilon_{yz} + a_{23}\varepsilon_{zz}, \quad (\text{A13})$$

$$a_{11} = \cos \lambda \sin \phi_s - \cos \delta \sin \lambda \cos \phi_s, \quad (\text{A14})$$

$$a_{12} = \cos \lambda \cos \phi_s + \cos \delta \sin \lambda \sin \phi_s, \quad (\text{A15})$$

$$a_{13} = \sin \lambda \sin \delta, \quad (\text{A16})$$

$$a_{21} = \sin \delta \cos \phi_s, \quad (\text{A17})$$

$$a_{22} = -\sin \delta \sin \phi_s, \quad (\text{A18})$$

$$a_{23} = \cos \delta. \quad (\text{A19})$$

A5. Contribution Ratio From the Area Above the Target Point

As mentioned in section A1.2, if the hypocenter was deeper than 1 km, the contribution from grid cells within 0.0001° was disregarded. We demonstrate the adequacy of this procedure in this section. For simplicity, we consider a surface vertical point loading problem on the semiinfinite homogeneous half-space of a perfect elastic body (Boussinesq approximation). We estimate the ratio of the contribution from the area within radius R above the hypocenter to the contribution from the whole plane. Here, we consider the volumetric strain as representative of physical quantities that decay in proportion to $1/(a\theta)^2$, such as strain or tilt. Volumetric strain in the medium for the surface vertical point load is represented as follows in cylindrical coordinates (r, θ, z):

$$E_{\text{vol}} = \frac{1}{2\pi\eta} \frac{z}{(r^2 + z^2)^{3/2}}, \quad (\text{A20})$$

where z is the depth, r is the horizontal distance from the loading point, and $\eta = \lambda_L + \mu_L$ (Kamigaichi, 1998). If it is assumed that the loading mass density ρ is distributed uniformly on the surface of a semiinfinite medium, then the contribution from the area within radius R is

$$E_{\text{vol}} = \frac{\rho g}{2\pi\eta} \int_0^{2\pi} \int_0^R \frac{z}{(r^2 + z^2)^{3/2}} r dr d\phi = \frac{\rho g}{\eta} \left\{ 1 - \cos \left(\arctan \left(\frac{R}{z} \right) \right) \right\}. \quad (\text{A21})$$

Thus, the ratio of the contribution from the area within R to the contribution from the whole plane ($R \rightarrow \infty$) is $1 - \cos \left(\arctan \left(\frac{R}{z} \right) \right)$. When we set $R = 100$ m, this contribution ratio is about 90% at $z = 10$ m, 30% at

$z = 100$ m, and 0.5% at $z = 1,000$ m. Therefore, if $(R/z) < 0.1$, the contribution of the area within R from the epicenter is less than 0.5% and can be disregarded. Note that the relative contribution from the vicinity of the loading point of physical quantities that decay proportionally to $1/a\theta$, such as displacement, becomes much smaller than that for strain or tilt.

Acknowledgments

We thank Hiroshi Tsuruoka and Sachiko Tanaka for their assistance with our calculation programs to estimate strain and stress associated with the Earth tide. This manuscript was greatly improved by careful reviews of anonymous reviewers. We thank the Global CMT Project for providing the CMT catalog (<https://www.globalcmt.org/CMTfiles.html>). Plate boundary data at the Earth's surface were taken from Bird (2003, <https://agupubs.onlinelibrary.wiley.com/doi/full/10.1029/2001GC000252>). Isodepth contour data were taken from <https://earthquake.usgs.gov/data/slab/>. Plate convergence rate data were calculated by Plate Motion Calculator on the website of UNAVCO (<https://www.unavco.org/>). Figures were prepared using GMT (Wessel et al., 2013). The new program "TidalStrain" that we developed to calculate theoretical tidal strain and stress are open to the public on Meteorological Research Institute repository (<https://mri-2.mri-jma.go.jp/owncloud/index.php/s/deL4fhBdRj1srzx> or <https://mri-2.mri-jma.go.jp/nextcloud/index.php/s/deL4fhBdRj1srzx>).

References

- Aki, K., & Richards, P. G. (2002). *Quantitative seismology*, (2nd ed. p. 700). Sausalito: University Science Books.
- Ballance, P. F., Scholl, D. W., Vallier, T. L., & Herzer, R. H. (1989). Subduction of a late Cretaceous seamount of the Louisville ridge at the Tonga trench: A model of normal and accelerated tectonic erosion. *Tectonics*, *8*(5), 953–962. <https://doi.org/10.1029/TC008i005p00953>
- Bird, P. (2003). An updated digital model of plate boundaries. *Geochemistry, Geophysics, Geosystems*, *4*(3), 1027. <https://doi.org/10.1029/2001GC000252>
- Cloos, M., & Shreve, R. L. (1996). Shear-zone thickness and the seismicity of Chilean- and Marianas-type subduction zones. *Geology*, *24*(2), 107–110. [https://doi.org/10.1130/0091-7613\(1996\)024<0107:SZTATS>2.3.CO;2](https://doi.org/10.1130/0091-7613(1996)024<0107:SZTATS>2.3.CO;2)
- Cocco, M., & Rice, J. R. (2002). Pore pressure and poroelasticity effects in Coulomb stress analysis of earthquake interactions. *Journal of Geophysical Research*, *107*(B2), 2030. <https://doi.org/10.1029/2000JB000138>
- Crawford, W. C., Hildebrand, J. A., Dorman, L. M., Webb, S. C., & Wiens, D. A. (2003). Tonga Ridge and Lau Basin crustal structure from seismic refraction data. *Journal of Geophysical Research*, *108*(B4), 2195. <https://doi.org/10.1029/2001JB001435>
- Dziewonski, A. M., & Anderson, D. L. (1981). Preliminary reference Earth model. *Physics of the Earth and Planetary Interiors*, *25*(4), 297–356. [https://doi.org/10.1016/0031-9201\(81\)90046-7](https://doi.org/10.1016/0031-9201(81)90046-7)
- Dziewonski, A. M., Chou, T.-A., & Woodhouse, J. H. (1981). Determination of earthquake source parameters from waveform data for studies of global and regional seismicity. *Journal of Geophysical Research*, *86*(B4), 2825–2852. <https://doi.org/10.1029/JB086iB04p02825>
- Ekström, G., Nettles, M., & Dziewonski, A. M. (2012). The global CMT project 2004–2010: Centroid-moment tensors for 13,017 earthquakes. *Physics of the Earth and Planetary Interiors*, *200–201*, 1–9. <https://doi.org/10.1016/j.pepi.2012.04.002>
- Farrell, W. E. (1972). Deformation of the Earth by surface loads. *Reviews of Geophysics and Space Physics*, *10*(3), 761–797. <https://doi.org/10.1029/RG010i003p00761>
- Flinn, E. A., Engdahl, E. R., & Hill, A. R. (1974). Seismic and geographical regionalization. *Bulletin of the Seismological Society of America*, *64*, 771–993.
- Fujiwara, T., Yamazaki, T., & Joshima, M. (2001). Bathymetry and magnetic anomalies in the Havre Trough and southern Lau Basin: from rifting to spreading in back-arc basins. *Earth and Planetary Science Letters*, *185*(3–4), 253–264. [https://doi.org/10.1016/S0012-821X\(00\)00378-2](https://doi.org/10.1016/S0012-821X(00)00378-2)
- Gilbert, F., & Dziewonski, A. M. (1975). An application of normal mode theory to the retrieval of structural parameters and source mechanisms from seismic spectra. *Philosophical Transactions of the Royal Society of London. Series A, Mathematical and Physical Sciences*, *278*(1280), 187–269. <https://doi.org/10.1098/rsta.1975.0025>
- Gutenberg, B., & Richter, C. F. (1944). Frequency of earthquakes in California. *Bulletin of the Seismological Society of America*, *34*, 185–188.
- Hayes, G. P., Wald, D. J., & Johnson, R. L. (2012). Slab1.0: A three-dimensional model of global subduction zone geometries. *Journal of Geophysical Research*, *117*, B01302. <https://doi.org/10.1029/2011JB008524>
- Heaton, T. H. (1975). Tidal triggering of earthquakes. *Geophys. J. R. astr. Soc.*, *43*(2), 307–326. <https://doi.org/10.1111/j.1365-246X.1975.tb00637.x>
- Ide, S. (2013). The proportionality between relative plate velocity and seismicity in subduction zones. *Nature Geoscience*, *6*(9), 780–784. <https://doi.org/10.1038/NGEO1901>
- Ide, S., & Tanaka, Y. (2014). Controls on plate motion by oscillating tidal stress: Evidence from deep tremors in western Japan. *Geophysical Research Letters*, *41*, 3842–3850. <https://doi.org/10.1002/2014GL060035>
- Ide, S., Yabe, S., & Tanaka, Y. (2016). Earthquake potential revealed by tidal influence on earthquake size-frequency statistics. *Nature Geoscience*, *9*(11), 834–837. <https://doi.org/10.1038/NGEO2796>
- Kamigaichi, O. (1998). Green functions of the earth at borehole sensor installation depths for surface point load. *Papers in Meteorology and Geophysics*, *48*(4), 89–100. <https://doi.org/10.2467/mripapers.48.89>
- Lallemand, S. E., Malavieille, J., & Calassou, S. (1992). Effects of oceanic ridge subduction on accretionary wedges: Experimental modeling and marine observations. *Tectonics*, *11*(6), 1301–1313. <https://doi.org/10.1029/92TC00637>
- Matsumoto, K., Sato, T., Takanezawa, T., & Ooe, M. (2001). GOTIC2: A program for computation of oceanic tidal loading effect. *Journal of the Geodetic Society of Japan*, *47*, 243–248.
- Matsumoto, K., Takanezawa, T., & Ooe, M. (2000). Ocean tide models developed by assimilating TOPEX/POSEIDON altimeter data into hydrodynamical model: A global model and a regional model around Japan. *Journal of Oceanography*, *56*(5), 567–581. <https://doi.org/10.1023/A:1011157212596>
- Mochizuki, K., Yamada, T., Shinohara, M., Yamanaka, Y., & Kanazawa, T. (2008). Weak interplate coupling by seamounts and repeating $M \sim 7$ earthquakes. *Science*, *321*(5893), 1194–1197. <https://doi.org/10.1126/science.1160250>
- Nakai, S. (1979). Subroutine program for computing the tidal forces for the practical use (in Japanese with English abstract). *Proceedings of the International Latitude Observatory of Mizusawa*, *18*, 124–135.
- Nishikawa, T., & Ide, S. (2015). Background seismicity rate at subduction zones linked to slab-bending-related hydration. *Geophysical Research Letters*, *42*, 7081–7089. <https://doi.org/10.1002/2015GL064578>
- Noda, H., Nakatani, M., & Takane, H. (2013). Large nucleation before large earthquakes is sometimes skipped due to cascade-up—Implications from a rate and state simulation of faults with hierarchical asperities. *Journal of Geophysical Research: Solid Earth*, *118*, 1345–1362. <https://doi.org/10.1002/jgrb.50122>
- Obara, K., & Kato, A. (2016). Connecting slow earthquakes to huge earthquakes. *Science*, *353*(6296), 253–257. <https://doi.org/10.1126/science.aaf1512>
- Ozawa, I. (1974). Types and distribution patterns of earth tides (in Japanese with English abstract). *Journal of the Geodetic Society of Japan*, *20*, 178–187.
- Parson, L. M., & Wright, I. C. (1996). The Lau-Havre-Taupo back-arc basin: A southward-propagating, multi-stage evolution from rifting to spreading. *Tectonophysics*, *263*(1–4), 1–22. [https://doi.org/10.1016/S0040-1951\(96\)00029-7](https://doi.org/10.1016/S0040-1951(96)00029-7)

- Scholz, C. H. (1968). The frequency-magnitude relation of microfracturing in rock and its relation to earthquakes. *Bulletin of the Seismological Society of America*, *58*, 399–415.
- Scholz, C. H. (2015). On the stress dependence of the earthquake b value. *Geophysical Research Letters*, *42*, 1399–1402. <https://doi.org/10.1002/2014GL062863>
- Scholz, C. H., & Small, C. (1997). The effect of seamount subduction on seismic coupling. *Geology*, *25*(6), 487–490. [https://doi.org/10.1130/0091-7613\(1997\)025<0487:TEOSSO>2.3.CO;2](https://doi.org/10.1130/0091-7613(1997)025<0487:TEOSSO>2.3.CO;2)
- Schorlemmer, D., Wiemer, S., & Wyss, M. (2005). Variations in earthquake-size distribution across different stress regimes. *Nature*, *437*(7058), 539–542. <https://doi.org/10.1038/nature04094>
- Schuster, A. (1897). On lunar and solar periodicities of earthquakes. *Proceedings of the Royal Society of London*, *61*, 455–465.
- Takanezawa, T., Matsumoto, K., Ooe, M., & Naito, I. (2001). Effects of the long-period ocean tide on Earth rotation, gravity and crustal deformation predicted by global barotropic model: periods from Mtm to Sa. *Journal of the Geodetic Society of Japan*, *47*, 545–550.
- Tanaka, S., Ohtake, M., & Sato, H. (2002a). Evidence for tidal triggering of earthquakes as revealed from statistical analysis of global data. *Journal of Geophysical Research*, *107*(B10), 2211. <https://doi.org/10.1029/2001JB001577>
- Tanaka, S., Ohtake, M., & Sato, H. (2002b). Spatio-temporal variation of the tidal triggering effect on earthquake occurrence associated with the 1982 South Tonga earthquake of M_w 7.5. *Geophysical Research Letters*, *29*(16), 3-1–3-4. <https://doi.org/10.1029/2002GL015386>
- Taylor, B., Zellmer, K., Martinez, F., & Goodliffe, A. (1996). Sea-floor spreading in the Lau back-arc basin. *Earth and Planetary Science Letters*, *144*(1-2), 35–40. [https://doi.org/10.1016/0012-821X\(96\)00148-3](https://doi.org/10.1016/0012-821X(96)00148-3)
- Tsuruoka, H., Ohtake, M., & Sato, H. (1995). Statistical test of the tidal triggering of earthquakes: contribution of the ocean tide loading effect. *Geophysical Journal International*, *122*(1), 183–194. <https://doi.org/10.1111/j.1365-246X.1995.tb03546.x>
- Turner, S., & Hawkesworth, C. (1998). Using geochemistry to map mantle flow beneath the Lau Basin. *Geology*, *26*(11), 1019–1022. [https://doi.org/10.1130/0091-7613\(1998\)026<1019:UGTMMF>2.3.CO;2](https://doi.org/10.1130/0091-7613(1998)026<1019:UGTMMF>2.3.CO;2)
- Uchida, N., Iinuma, T., Nadeau, R. M., Bürgmann, R., & Hino, R. (2016). Periodic slow slip triggers megathrust zone earthquakes in northeastern Japan. *Science*, *351*(6272), 488–492. <https://doi.org/10.1126/science.aad3108>
- Utsu, T. (1999). Representation and analysis of the earthquake size distribution: A historical review and some new approaches. *Pure and Applied Geophysics*, *155*(2-4), 509–535. <https://doi.org/10.1007/s000240050276>
- Wessel, P., Smith, W. H. F., Scharroo, R., Luis, J., & Wobbe, F. (2013). Generic Mapping Tools: Improved Version Released. *Eos, Transactions American Geophysical Union*, *94*(45), 409–410. <https://doi.org/10.1002/2013EO450001>